2-7-2008

Characterization of spectral response of a quantum dots-in-a-well infrared focal plane array

Michael Lenz II

Michael C Lenz II
Candidate

Electrical and Computer Engineering
Department

This thesis is approved, and it is acceptable in quality and form for publication on microfilm:

Approved by the Thesis Committee:

Dr. Sanjay Krishna , Chairperson

Dr. Steven Brueck

Dr. Ralph Dawson

Dr. Luke Lester

Accepted:

Dean, Graduate School

Date

Characterization of Spectral Response of a Quantum Dots-in-a-Well Infrared Focal Plane Array

BY

Michael C Lenz II

Bachelor of Science in Electrical Engineering
University of New Mexico, May 2005

THESIS

Submitted in Partial Fulfillment of the
Requirements for the Degree of

Master of Science
Electrical Engineering

The University of New Mexico
Albuquerque, New Mexico

DECEMBER 2007

DEDICATIONS

To my wonderful wife, Elena, for her understanding and support. Thank you to my parents for instilling the values of hard work and perseverance.

ACKNOWLEDGEMENTS

I would like to thank my advisor, Dr. Sanjay Krishna, for giving me direction as an undergraduate and stoking my interest to attend graduate school. His support and guidance over the course of this work was instrumental to my success. I would also like to thank Dr. Jay Brown, Dr. Jean-Baptiste Rodriguez, Dr. Yagya Sharma, and Eric Varley for their contributions. Special thanks to Dr. John Hubbs and his group at Ball Aerospace & Technologies Corp. and Greg Pierce and Mark Stegall of SE-IR Corporation for their helpful conversations. Finally, I would like to thank my management team at Sandia National Laboratories: Rebecca Horton, Kevin Linker, Bill Rhodes, and Tommy Woodall, without whom I could have never realized my goals in higher education.

Characterization of Spectral Response of a Quantum Dots-in-a-Well Infrared Focal Plane Array

BY

Michael C Lenz II

ABSTRACT OF THESIS

Submitted in Partial Fulfillment of the
Requirements for the Degree of

Master of Science
Electrical Engineering

The University of New Mexico
Albuquerque, New Mexico

DECEMBER 2007

Characterization of Spectral Response of a
Quantum Dots-in-a-Well Infrared Focal Plane Array

by

Michael C Lenz II

Bachelor of Science in Electrical Engineering, University of New Mexico, May 2005
Master of Science in Electrical Engineering, University of New Mexico, December 2007

ABSTRACT

Spectral characterization of a novel single bump, two-color InAs/InGaAs quantum dots-in-a-well (DWELL) infrared focal plane array (FPA) was undertaken and reported here. The hypothesis of the study is that the FPA will exhibit bias-tunable spectral response. Broadband and two-color performance measures of the DWELL FPA are discussed and presented. The DWELL structure is a hybrid of a quantum dot (QD) photodetector consisting of an active region composed of InAs quantum dots embedded in InGaAs quantum wells. The DWELL FPA demonstrates mid-wave infrared (MWIR) and long-wave infrared (LWIR) performance believed to be attributed to transitions from bound states in the dot to higher and lower lying energy states in the quantum well, respectively. The DWELL samples were grown by molecular beam epitaxy (MBE) and fabricated into 320 x 256 focal plane arrays with indium bumps via standard lithography at the University of New Mexico (UNM). The samples were hybridized to Indigo Systems Corporation ISC9705 read out integrated circuits and investigated with a SE-IR Corporation CamIRa™ test system. The DWELL FPA exhibited temporal noise equivalent difference in temperature (NEDT) values of 43mK and 63mK (MWIR and LWIR respectively) at 77K.

Table of Contents

Table of Figures x
List of Tables xii
Acronyms xiii
1 Introduction to Infrared Detection 1
1.1 Photodetector Types 2
1.2 Spectral Response of Photon Detectors 4
1.3 Document Outline 7
2 Bandgap Engineered IR Photodetectors 9
2.1 Quantum Well Infrared Photodetectors 11
2.2 Quantum Dot Infrared Photodetectors 13
2.3 Quantum Dots-in-a-Well Infrared Photodetectors 15
2.4 Quantum Dots-in-a-Well (DWELL) Infrared Focal Plane Array (FPA) 19
2.5 Fabrication of the DWELL FPA 20
3 Materials and Methods 22
3.1 Indigo Systems Corporation ISC9705 Readout Integrated Circuit 22
3.1.1 Calculating Detector Bias 23
3.1.2 ROIC Gain Setting 26
3.2 SE-IR CamIRa™ Data Acquisition Setup 27
3.3 DWELL FPA Performance Measurements 28
3.3.1 FPA Temporal Noise Measurement 28
3.3.1.1 FPA Camera System Noise Measurement 30
3.3.1.2 Total Noise Measurement 31
3.3.1.3 Sources of Readout Noise 33
3.3.2 Spatial Noise Measurements 34
3.4 FPA Spectral Response Measurements 36
3.4.1 FPA Spectral Response Test Setup 37
3.4.2 FPA Spectral Response Results 40
4 Broadband Figures of Merit 43
4.1 Responsivity 46
4.2 Noise Equivalent Power 47
4.3 Noise Equivalent Irradiance 49
4.4 Detectivity 51
4.5 Noise Equivalent Difference in Temperature (NEDT) 54
4.6 Brief Comparison to State of the Art Devices 56
5 Two-Color Performance 58
5.1 Mid-Wave and Long-Wave IR Noise Measurements 58
5.2 Responsivity 60
5.3 Noise Equivalent Power (NEP) 63
5.4 Noise Equivalent Irradiance (NEI) 64
5.5 Detectivity (D*) 65
5.6 Noise Equivalent Difference in Temperature (NEDT) 66
5.7 Review of Two-Color Performance 67

6 Future Work and Conclusions 69
6.1 Exploring FPA Spectral Diversity 69
6.2 Comparison of the DWELL FPA to HgCdTe Two-Color Detectors 72
6.3 Conclusions 73
7 Previously Published Work 76
List of Appendices 77
Appendix A. Two-Color Noise Equivalent Power (NEP) Plots 78
Appendix B. Two-Color Noise Equivalent Irradiance (NEI) 80
Appendix C. Two-Color Detectivity Plots 82
Appendix D. Two-Color Noise Equivalent Difference in Temperature (NEDT) Plots 84
References 86

Table of Figures

Figure 1. Atmospheric Infrared Light Transmission as a Function of Wavelength [25]... 1
Figure 2. Absorption Coefficients for Various Semiconductor Materials [6] 5
Figure 3. An Illustration of the Differences between Interband and Intersubband Energy Transitions..... 7
Figure 4. Bandgap and Cutoff Wavelength of Several Semiconductor Systems [23]..... 10
Figure 5. Schematic of the QWIP Structure 12
Figure 6. Quantum Well Energy Band Diagram 13
Figure 7. Schematic of the QDIP Structure 15
Figure 8. Schematic of the Single Pixel DWELL Structure 16
Figure 9. DWELL Energy Diagram Illustrating: (i.) Bound-to-Bound, (ii.) Bound-to-Quasi-bound, and (iii.) Bound-to-Continuum Transitions..... 17
Figure 10. Measured Spectral Response of an InAs/InGaAs DWELL Demonstrating MWIR, LWIR and VLWIR Responses from Bound-to-Continuum, Bound-to-Quasi-bound, and Bound-to-Bound Transitions, respectively [9]..... 18
Figure 11. Diagram of the InAs/InGaAs DWELL [9] 19
Figure 12. Schematic of a DWELL FPA Pixel..... 20
Figure 13. SEM Image of the DWELL FPA with In Bumps..... 21
Figure 14. FPA Direct Injection Unit Cell..... 23
Figure 15. PMOS Source-to-Gate Voltage Versus Drain Current..... 25
Figure 16. Block Diagram of the CamIRa™ System 27
Figure 17. FPA Temporal RMS Noise Voltage versus Number of Frames 29
Figure 18. SE-IR CamIRa™ System Noise Voltage 31
Figure 19. FPA Noise versus Photon Irradiance at 77K..... 32
Figure 20. Non-Uniformity Correction Example..... 35
Figure 21. Images Captured Without and With NUC (left and right, respectively)..... 36
Figure 22. FPA Spectral Response Measurement Setup 38
Figure 23. Usage of Monochromator Gratings in FPA Spectral Response Measurements. 39
Figure 24. Usage of Long-wave Pass Filters in FPA Spectral Response Measurements. 39
Figure 25. FPA Response versus Wavelength (Trial 1). 41
Figure 26. FPA Response versus Wavelength (Trial 2). 41
Figure 27. Spectral Response of a Typical DWELL Detector..... 42
Figure 28. Output Voltage versus Irradiance for the DWELL FPA at 77K 44
Figure 29. Detector Noise Variance versus Output at 77K 46
Figure 30. NEP versus Irradiance at 77K 49
Figure 31. NEI versus Irradiance at 77K 51
Figure 32. Detectivity versus Irradiance at 77K 52
Figure 33. BLIP Detectivity for QE Estimation at 77K..... 54
Figure 34. NEDT versus FPA Output Voltage at 77K 55
Figure 35. DWELL FPA MWIR Noise versus Irradiance at 77K..... 59
Figure 36. DWELL FPA LWIR Noise versus Irradiance at 77K..... 59
Figure 37. MWIR and LWIR Output Voltage versus Irradiance at 77K..... 60
Figure 38. MWIR Output Voltage versus Irradiance at 77K..... 61

Figure 39. LWIR Output Voltage versus Irradiance at 77K 61
Figure 40. MWIR Responsivity versus Irradiance at 77K 62
Figure 41. LWIR Responsivity versus Irradiance at 77K 62
Figure 42. Exploring the IR Retina: Response of the Cones in a Human Eye May be Mimicked by Spectral Diversity within the Pixels of the DWELL FPA 70
Figure 43. Response from Selected FPA Pixels at a Detector Bias of -0.5V. 71
Figure 44. HgCdTe Two-Color Single Pixel Detector [19]. 73
Figure 45. DWELL Energy Bands at Different Biases 74
Figure 46. MWIR and LWIR NEP at V_{DB} ~0.5V and 77K 78
Figure 47. MWIR and LWIR NEP at V_{DB} ~0.75V and 77K 78
Figure 48. MWIR and LWIR NEP at V_{DB} ~1.0V and 77K 79
Figure 49. MWIR and LWIR NEP at V_{DB} ~1.1V and 77K 79
Figure 50. MWIR and LWIR NEI at V_{DB} ~0.5V and 77K 80
Figure 51. MWIR and LWIR NEI at V_{DB} ~0.75V and 77K 80
Figure 52. MWIR and LWIR NEI at V_{DB} ~1.0V and 77K 81
Figure 53. MWIR and LWIR NEI at V_{DB} ~1.1V and 77K 81
Figure 54. MWIR and LWIR Detectivity at V_{DB} ~0.5V and 77K 82
Figure 55. MWIR and LWIR Detectivity at V_{DB} ~0.75V and 77K 82
Figure 56. MWIR and LWIR Detectivity at V_{DB} ~1.0V and 77K 83
Figure 57. MWIR and LWIR Detectivity at V_{DB} ~1.1V and 77K 83
Figure 58. MWIR and LWIR NEDT at V_{DB} ~0.5V and 77K 84
Figure 59. MWIR and LWIR NEDT at V_{DB} ~0.75V and 77K 84
Figure 60. MWIR and LWIR NEDT at V_{DB} ~1.0V and 77K 85
Figure 61. MWIR and LWIR NEDT at V_{DB} ~1.1V and 77K 85

List of Tables

Table 1. Bandgap and Cutoff Wavelengths of Common Semiconductors 9
Table 2. Indigo 9705 Bias Range 24
Table 3. Estimate of ΔV_{SG} Values 26
Table 4. Conversion Gain Experiment Results 27
Table 5. FPA Readout Integration Times 32
Table 6. Optimum Operating Range of Long-wave Pass Filters [from Spectrogon, Inc]. 38
Table 7. Optimum Operating Range of Monochromator Gratings [from PIActon, Inc]. 38
Table 8. $C_G G$ Conversion Gain Product Estimates at 77K 46
Table 9. Responsivity Values at 77K 47
Table 10. Minimum Recorded NEP Results at 77K 49
Table 11. Minimum Recorded NEI Results at 77K 50
Table 12. Peak Detectivity Results at 77K 52
Table 13. Minimum NEDT Results at 77K 56
Table 14. NEDT and D* Values of Different State of the Art IR Detectors [2]. 56
Table 15. MWIR and LWIR Responsivity Results at 77K 63
Table 16. MWIR and LWIR Minimum NEP Values at 77K 64
Table 17. MWIR and LWIR Minimum NEI Values at 77K 64
Table 18. Maximum MWIR and LWIR Detectivity at 77K 65
Table 19. Average Measured Detectivity 66
Table 20. Minimum MWIR and LWIR NEDT at 77K 67

Acronyms

A/D	analog-to-digital
AR	anti-reflective
ADC	analog-to-digital counts
BLIP	background limited infrared photodetector
CCD	charge coupled device
C_G	conversion gain
DWELL	dots-in-a-well
D^*	detectivity
EHP	electron-hole pair
E_e	photon irradiance (power)
E_q	photon irradiance (number of photons)
FPA	focal plane array
HgCdTe	mercury cadmium telluride
IR	infrared
LWIR	long wave infrared (8-12μm)
MBE	molecular beam epitaxy
MOCVD	metal-organic chemical vapor deposition
MWIR	mid-wave infrared (3-5μm)
NEDT	noise equivalent difference in temperature
NEI	noise equivalent irradiance
NEP	noise equivalent power
NUC	non-uniformity correction
PV	photovoltaic
QDIP	quantum dot infrared photodetector
QE	quantum efficiency
QWIP	quantum well infrared photodetector
RMS	root mean square
ROIC	readout integrated circuit
SNR	signal-to-noise ratio
T_{int}	integration time
VLWIR	very long wave infrared (>12μm)
V_{DB}	detector bias voltage
V_{DETCOM}	voltage bias applied to array pixels
V_n	noise voltage
V_{output}	output voltage

Chapter 1

1 Introduction to Infrared Detection

In nature, there exist convenient windows of atmospheric transmission of infrared (IR) light. Two of these transmission windows fall between ~3-5μm and ~8-14μm (see Figure 1). Due to this atmospheric transmission, infrared photodetectors are widely used today in a variety of terrestrial applications covering many fields such as spectroscopy, motion detection, thermal imaging, satellite imaging, distance ranging and missile defense. Though these applications are very different and diverse on the surface, they are all based upon the principle that infrared photons incident on a detector cause an electrical change that can be measured. It is this measured physical change that is used as a signal for detection of IR light. The change utilized as a signal varies on the type of infrared detector, which is discussed below.

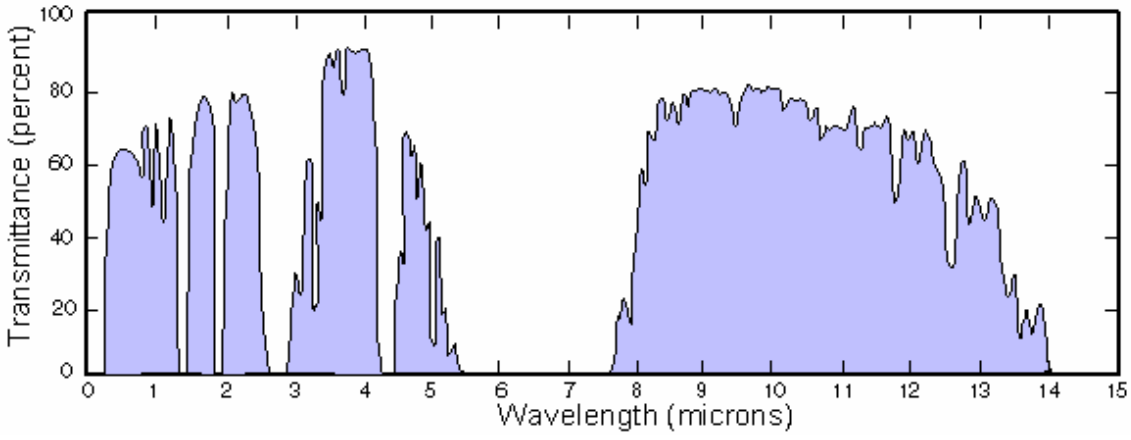

Figure 1. Atmospheric Infrared Light Transmission as a Function of Wavelength [25]

1.1 Photodetector Types

There are three major types of infrared photodetectors: 1) photoconductor photon detectors, 2) photovoltaic (PV) photon detectors, and 3) thermal detectors. Photoconductor detectors can be made of intrinsic (undoped) or extrinsic (doped) semiconductor materials. Photoconductors are named such because when a photon of sufficient energy is absorbed by the semiconductor material an electron-hole pair (EHP) is generated, resulting in a measurable change in the detector conductivity. Operation of a photoconductor detector consists of applying an external voltage bias across the detector material and measuring the current through the device. Under normal circumstances, an undesirable current, called dark current, exists due to the thermal generation of carriers (i.e., not due to absorption of photons that generate electron-hole pairs). This dark current is a noise source that must be suppressed. Photoconductors are usually cooled to cryogenic temperatures to reduce the thermal generation of carriers, thus reducing dark current. The desired signal to measure from a photoconductor is an increase in series current caused by the increased semiconductor material's conductivity resulting from the absorption of incident photons. Photoconductor resistance (R_d) is inversely proportional to the incident photon flux (Φ_q) [4],

Equation 1

$$R_d \propto \frac{1}{\Phi_q}.$$

Photoconductor detectors exhibit broad spectral response since the absorption of photons occurs when the photon energy (E_{ph}), which is directly related to photon wavelength (λ), is greater than or equal to the bandgap energy of the semiconductor material [6],

Equation 2

$$E_{ph} = \frac{hc}{\lambda}$$

where, Planck's constant h = 6.626 x 10^{-34} J-s and c is the speed of light [2.998 x 10^{8} m/s].

Photovoltaic detectors (also known as photodiodes) are made from extrinsic semiconductor materials that have been doped appropriately to create a p-n junction. An incident photon with energy greater than the band gap of the semiconductor is absorbed near the junction, causing an electron to be raised to the conduction band, resulting in the formation of an EHP (shown in Figure 3). The result is a measurable voltage, or current, that is the signal indicating the absorption of photons of energy equal to, or greater than, the bandgap of the semiconductor material. Despite being more fragile than photoconductors, PV devices have a better theoretical signal-to-noise ratio, are simpler to bias, and have a more accurately predictable responsivity than photoconductors, which exhibit high resistance at low backgrounds, requiring a modification of the predicted responsivity [24]. Like photoconductors, PV detectors generally have a broad spectral response because their output signal is due to the absorption of photons whose energy is greater than the material band gap. Photoconductors are used as light detectors in a wide range of applications and PV detectors can also be used in converting sunlight into electricity.

The third kind of devices, thermal detectors, indicate the absorption of infrared radiation by an increase in the surface temperature of the detector material. This increase in temperature results in a physical change in the material that can be measured. The change could be in the device electrical resistance, material expansion, or a generated voltage in a bi-metal junction, as in a thermocouple. Depending on the physical parameter to be measured, thermal detectors can made from a variety of materials, including semiconductors. In the case of a semiconductor material being used as a photon or thermal detector, the response time of a thermal detector is slower than that of a photon detector because the generation of an electron-hole pair is faster than the temperature change of the material. Thermal detectors exhibit broad spectral response, ranging from the visible to IR, since radiation absorption at the detector surface is not a strong function of wavelength (photon energy) [4]. An example of a thermal detector is a bolometer. Bolometers detect temperature increases due to incident radiant energy.

1.2 Spectral Response of Photon Detectors

The spectral response of a photon detector (either photoconductor or PV) is a function of the bandgap energy (E_g) and the absorption coefficient (α) of the semiconductor material. To absorb a photon and generate an EHP, the photon energy must at least be equal to the detector material's bandgap. The result is a simple relationship between the bandgap energy in electron volts (eV) and the longest detectable photon (cutoff) wavelength (λ_c), measured in microns [18],

Equation 3

$$\lambda_c = \frac{1.24}{E_g}.$$

This relation implies that for a given type of semiconductor, any photon(s) with energy equal to or greater than the material bandgap (i.e., any wavelength less than or equal to λ_c) will be detected. This is not the case, however. Photon absorption of a material is a function of wavelength and becomes very high for short wavelengths (high energy photons). Figure 2 illustrates the relationship between absorption and wavelength for several common types of semiconductor materials.

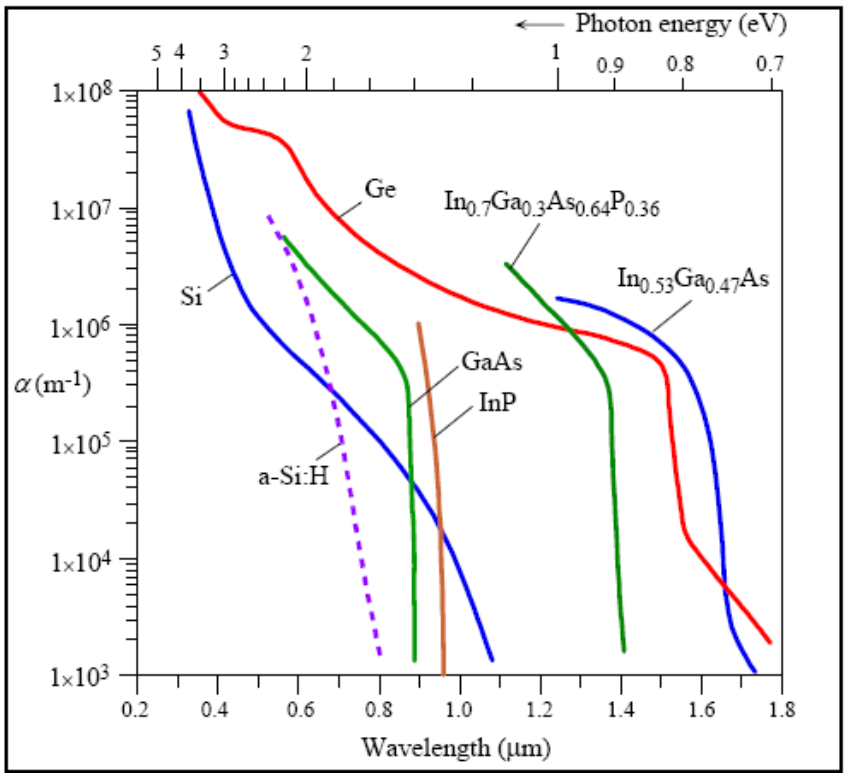

Figure 2. Absorption Coefficients for Various Semiconductor Materials [6]

Though photon absorption is increased at shorter wavelengths, not all absorbed photons generate an electron-hole pair that contribute to the measured signal current. This is because the increased absorption coefficient leads to absorption near the detector surface, where defects act as recombination centers [6]. This means that the conductivity, or output voltage or current is unchanged, limiting the detection of short wavelength

photons. Generation (g) of EHPs as a function of distance (x) into the material decays exponentially according to the absorption coefficient of a material [4],

Equation 4 $$g(x) = E_q \alpha \exp[-\alpha x]$$

where, E_q is photon irradiance [photons/sec-cm^2].

From this relation it can be seen that high energy (short wavelength) photons generate undetected EHPs near the surface of the material that recombine before being collected, limiting the spectral response of the detector. Another common limitation of the spectral response encountered with photon detectors is the use of anti-reflective (AR) coatings. It is common for detectors to have an AR coating on their surface to promote the absorption of photons. The AR coating by design transmits specific photon wavelengths, limiting the photon wavelengths transmitted to the photon detector, however. This further limits device spectral response. To address the shortcomings of homogeneous semiconductor infrared photon detectors, a class of band gap engineered materials has evolved. Band gap engineering allows detector designers to tailor device spectral response in an effort to optimize response for a given application. In these materials, intersubband transitions of charge carriers provide an effective band gap different from the band gap of homogeneous semiconductor device that utilizes interband transitions (i.e., charge carrier transitions across the material band gap, E_g). This arrangement allows designers to create LWIR detector devices. Figure 3 illustrates the difference between intersubband transitions (transitions within the conduction band, E_c) and interband transitions.

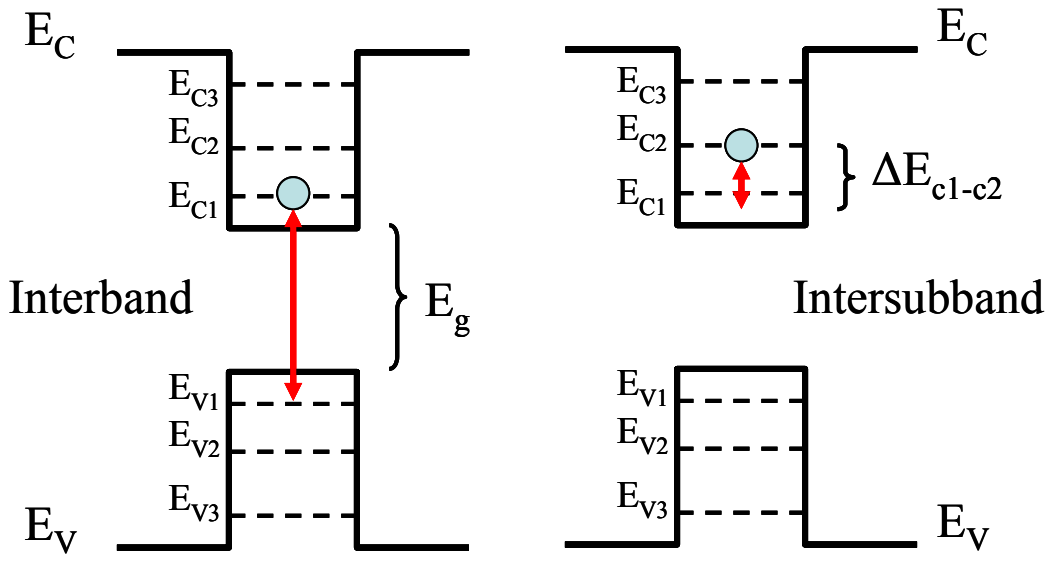

Figure 3. An Illustration of the Differences between Interband and Intersubband Energy Transitions

1.3 Document Outline

In this paper, the performance of the two-color quantum dots-in-a-well (DWELL) focal plane array is summarized. In this study the capability of measuring the spectral response of an FPA is established. The ability to measure FPA spectral response allows for the bias tunability of the FPA to be determined, as well as two-color figures of merit for the entire 320 x 256 array of detectors. The remaining sections of this manuscript that detail this investigation will proceed as follows:

1. **Chapter 2**: A background discussion of bandgap engineered photodetectors including the quantum well, quantum dot, and quantum dot-in-a-well structures.
2. **Chapter 3**: Presentation of performance measurements of a quantum dots-in-a-well focal plane array, including test methods and equipment used.

3. **Chapter 4**: Discussion of the broadband (no optics) performance of the quantum dots in a well focal plane array, including figures of merit.
4. **Chapter 5**: Discussion of the two-color performance of the quantum dots-in-a-well focal plane array, including figures of merit in both the MWIR and LWIR bands.
5. **Chapter 6**: Conclusions based on the preceding results and future work.

Chapter 2

2 Bandgap Engineered IR Photodetectors

Infrared photon detectors fabricated from single homogeneous semiconductor materials exhibit limited spectral response, as indicated previously by Equation 3. Cutoff wavelengths for several of the more commonly encountered semiconductors are listed below in Table 1. The inherent limitation to the spectral response of the above semiconductor materials has been overcome by infrared detector designers through the development of band gap engineered materials.

Table 1. Bandgap and Cutoff Wavelengths of Common Semiconductors

Semiconductor Material	Material Bandgap [eV]	Cutoff Wavelength, λ_c, [μm]
InSb	0.17	7.29
InAs	0.36	3.44
Ge	0.66	1.88
GaSb	0.72	1.72
Si	1.12	1.11
InP	1.35	0.92
GaAs	1.42	0.87
CdTe	1.56	0.79

Advances in semiconductor material growth methods, namely molecular beam epitaxy (MBE) and metal-organic chemical vapor deposition (MOCVD), have allowed designers to modify the spectral response characteristics of photoconductors by intermixing

semiconductor materials to alter the effective band gap of the materials. The change in band gap results in a change in the cutoff wavelength of the detector material, as illustrated by Equation 3. These heterogeneous materials systems are semiconductor alloys composed of two or more materials that enable a detector designer to create a photodetector with a desired λ_c within the constraints of the materials system. Figure 4 below shows the relationship between several heterogeneous semiconductor materials and band gap (and wavelength). With a given pair of materials, intermixing allows designers to create heterogeneous semiconductors with a specific band gap. For example, the GaAs/InAs materials allow for a heterogeneous material with a band gap between ~0.4 to 1.4 eV.

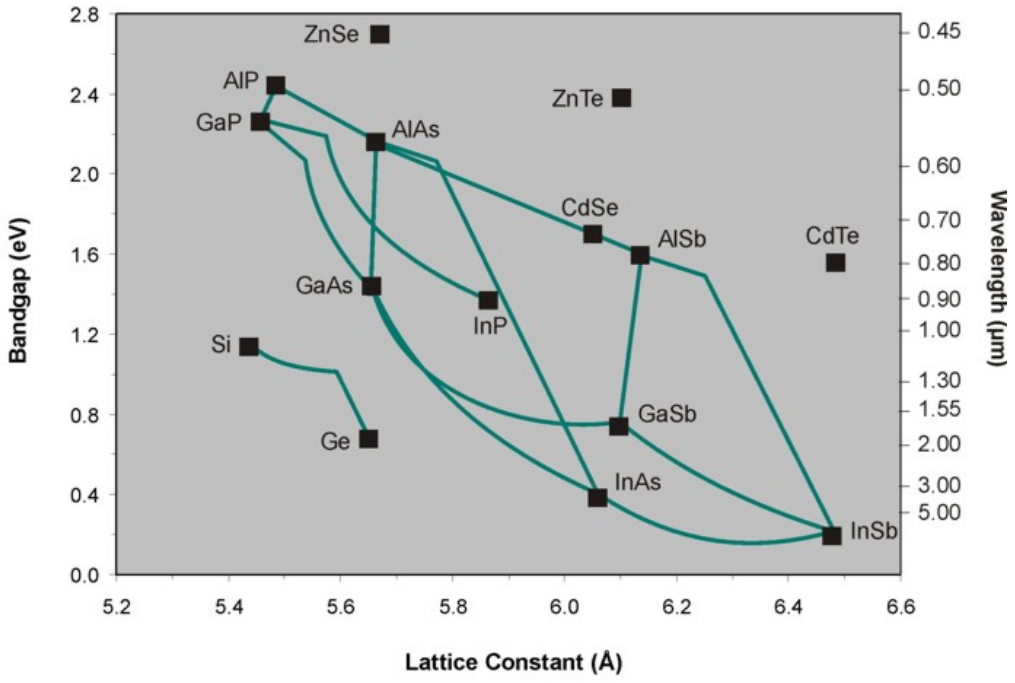

Figure 4. Bandgap and Cutoff Wavelength of Several Semiconductor Systems [23]

2.1 Quantum Well Infrared Photodetectors

The data presented in Figure 4 may give the notion that a photodetector of any desired spectral response may be created by using the appropriate portions of the proper materials to create a heterogeneous semiconductor alloy. This is not the case because there are practical limitations that do not allow for the combination of some materials. One example would be a designer attempting to create a long wave infrared detector (8 to 12μm). To do this a semiconductor material with a small band gap of approximately 0.12 to 0.15 eV would be required. When compared to larger band gap materials, small band gap materials are known to be more difficult to grow in large quantities and thus more difficult from which to fabricate devices [10]. This limitation sparked the development of photoconductive quantum well infrared photodetectors (QWIPs). A quantum well consists of a layer of material that has a narrow band gap which is sandwiched between two layers of a material with a larger band gap material (Figure 5). This arrangement of materials creates a small "effective band gap," due to quantum confinement, that allows for the absorption of LWIR photons. In a practical device, many layers of quantum wells are used to create the device active region, the region where a photon is absorbed and an electron is promoted to a higher energy state. This electron excitation caused by the absorption of a photon contributes to an increase in device conductivity. The material around the active region, known as the barrier, has a larger band gap and, therefore, does not absorb low energy photons. This barrier region acts as a window layer because it is composed of a higher band gap material, allowing photons to enter the active region (Figure 6).

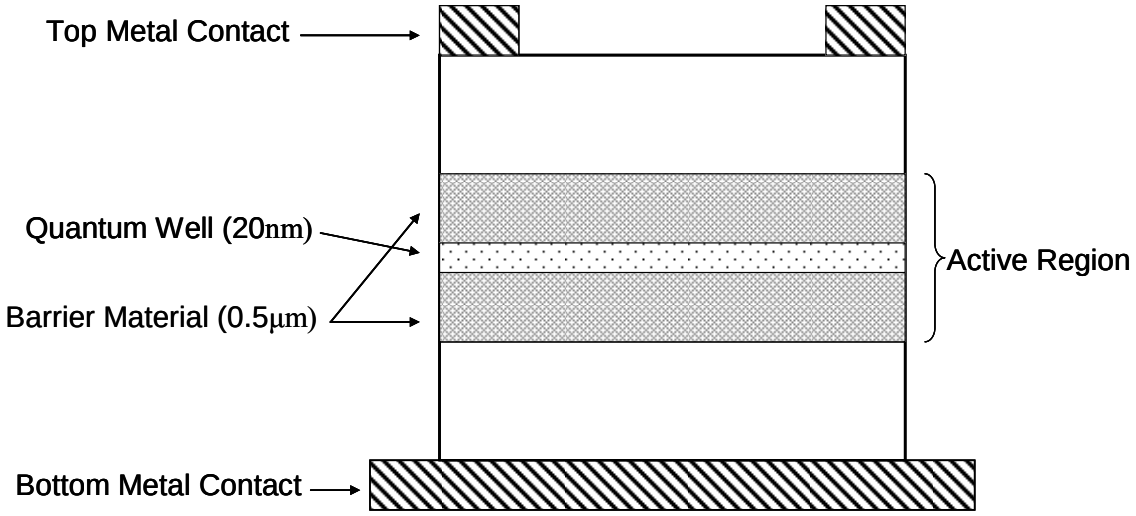

Figure 5. Schematic of the QWIP Structure

The absorption of low-energy photons in the active region of a QWIP is possible by intersubband absorption in the quantum well. Intersubband absorption occurs when an absorbed photon excites an electron via a transition from one allowed energy state to another without the electron being promoted to a state outside of the well, as illustrated in Figure 6, in which the electron gets promoted from E_{1e} to E_{2e}. The excitation occurs to and from the discrete energy levels that exist in a quantum well. Varying the width of the quantum well is a method to tune the spectral response of a QWIP from short wave infrared (SWIR) to LWIR response and beyond (to very long-wave infrared, VLWIR) [10].

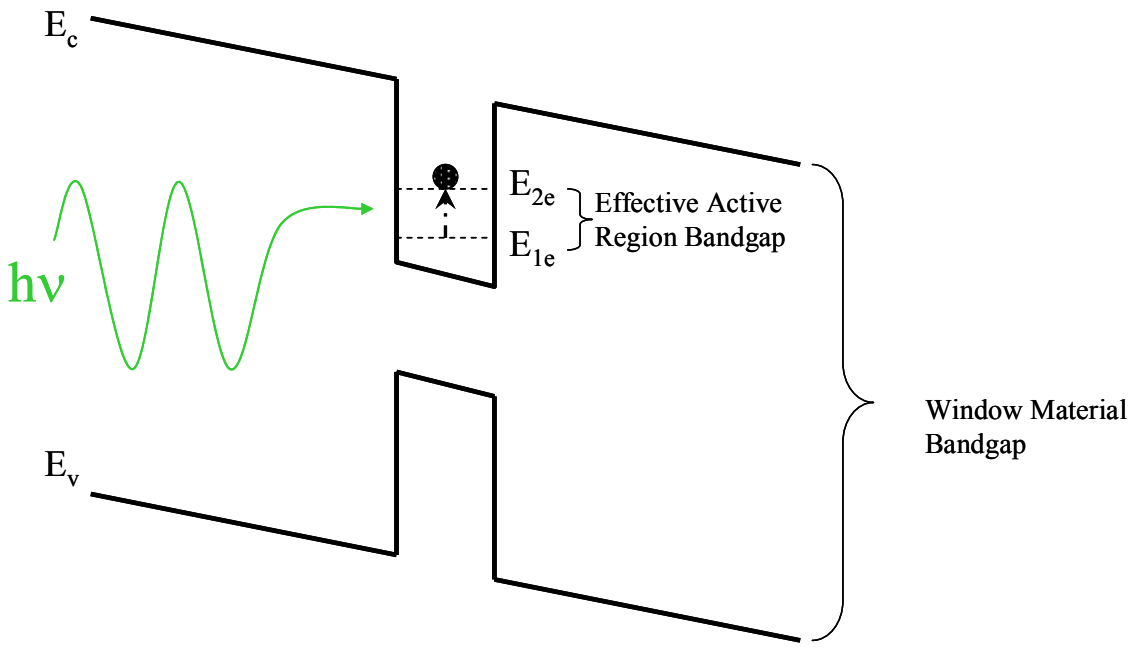

Figure 6. Quantum Well Energy Band Diagram

A limitation of QWIPs is that they are not inherently sensitive to photons that are polarized in the plane of the quantum well (i.e., normally incident light). For a photon to be absorbed, it must have a polarization component normal to the growth direction, meaning that QWIPs must be illuminated utilizing a 45 degree polished facet, or some other method of ensuring that some portion of any incident photons has a polarization component parallel to the quantum well growth direction [15].

2.2 Quantum Dot Infrared Photodetectors

A key step in the advancement of long-wave photodetectors came with the development of the device known as the quantum dot infrared photodetector, or QDIP. QDIPs offer several advantages over QWIPs. The three-dimensional carrier confinement of the QDIP makes the structure sensitive to normally incident light, and allows for a broader range of

spectral response because the QDs have several discrete energy states [11]. The QDIP also has the potential to exhibit lower dark (noise) current due to the low density of states as compared to the QWIP [1, 14]. For instance, QD density is around 10^{10}-10^{11}cm^{-2}, much lower than the typical equivalent sheet carrier doping concentration used in QWIPs [14]. QDIPs also have longer carrier lifetimes than QWIP devices because of reduced electron-hole scattering from a decreased level of electon-phonon interaction [7]. These are some key properties that led to the advancement of the QDIP over the past several years.

A quantum dot (QD) consists of a small volume of material that, when surrounded in all directions by a larger bandgap material, provides three-dimensional carrier confinement. This differs from the quantum well which offers only one dimensional carrier confinement. QDs are three dimensional structures grown by molecular beam epitaxy that "self-assemble" under the Stranski-Krastanov growth method due to lattice mismatch and the resulting strain in the growth materials [12]. Size and density of dots can be adjusted via the growth process, but the InAs QDs specifically used in the DWELL structure are typically on the order of 20nm at the base, 6-8nm in height and have an areal density of approximately 10^{10} cm^{-2}. To create a photodetector using quantum dots, thin layers containing the dots must be embedded in a larger bandgap material. Repeating this structure, in a manner similar to the QWIP, creates the device active region. An illustration is provided in Figure 7. It should be noted that adding layers of additional QDs is not a trivial task because it involves managing the excessive compressive strain associated with each QD layer [9].

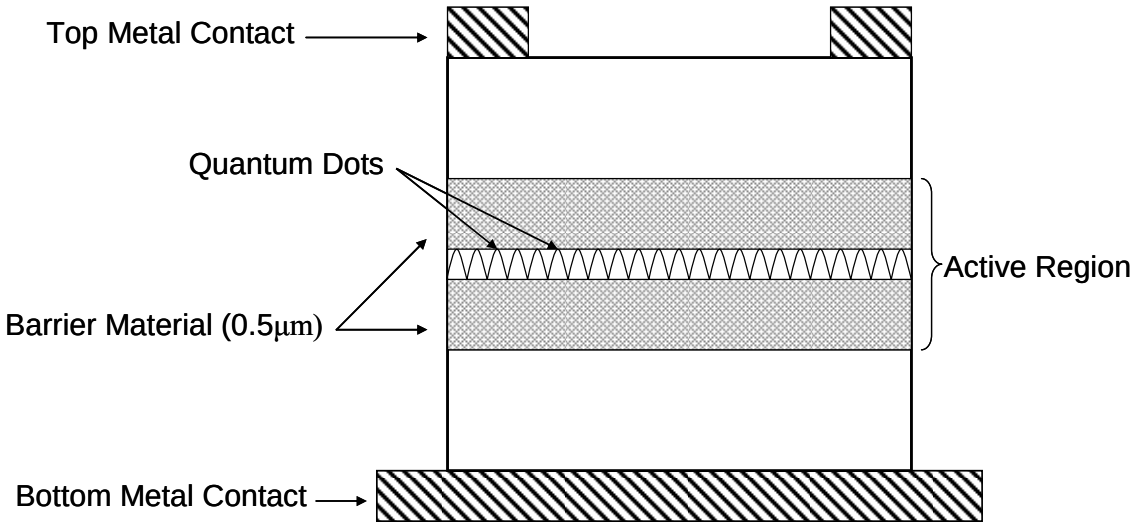

Figure 7. Schematic of the QDIP Structure

2.3 Quantum Dots-in-a-Well Infrared Photodetectors

The quantum dot-in-a-well photodetector structure is a hybrid of the QWIP and QDIP. The DWELL consists of an active region of quantum dots embedded inside a quantum well (shown in Figure 8). The DWELL structure can be used to make lasers, demonstrated by previous work at UNM by Lester, et al., though the emphasis here is on the DWELL as a photodetector. Through adjustment of the quantum well thickness, the DWELL structure allows for reproducible manipulation of the operating wavelength and the nature of energy transitions of the detector [9]. The DWELL structure also offers wide spectral response because of the possibility of the absorption of multiple energies. Photon absorption can occur by a few mechanisms: bound-to-bound transitions, bound-to-quasi-bound transitions, or bound-to-continuum transitions, see Figure 9. These transitions make it possible for the detection of photons from MWIR to VLWIR with a

single detector. Figure 10 shows the measured spectral response of an InAs/InGaAs DWELL [9] that demonstrates the detection of photons over the range of ~4 to 24μm. From these measurements, one can see the multi-color capability of the DWELL detector structure.

Multi-color detectors can provide benefit over single color detectors by offering spectral information in multiple bands, allowing for object discrimination and identification and providing improved temperature sensitivity. Present multi-spectral detectors are either based on multiple FPAs and a grating to sample different spectral regions of interest, or a broadband FPA with a spinning filter wheel [16]. An FPA created of multi-color detectors can provide for a simplified imaging system that does not require multiple FPAs or other filtering. The DWELL FPA is one promising technology that can offer the benefit of multi-color information from a single array.

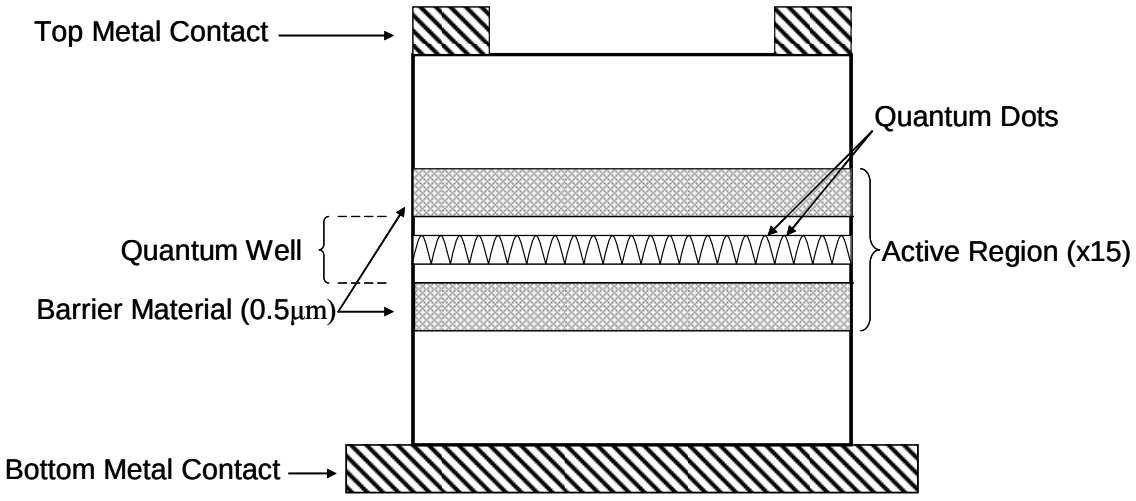

Figure 8. Schematic of the Single Pixel DWELL Structure

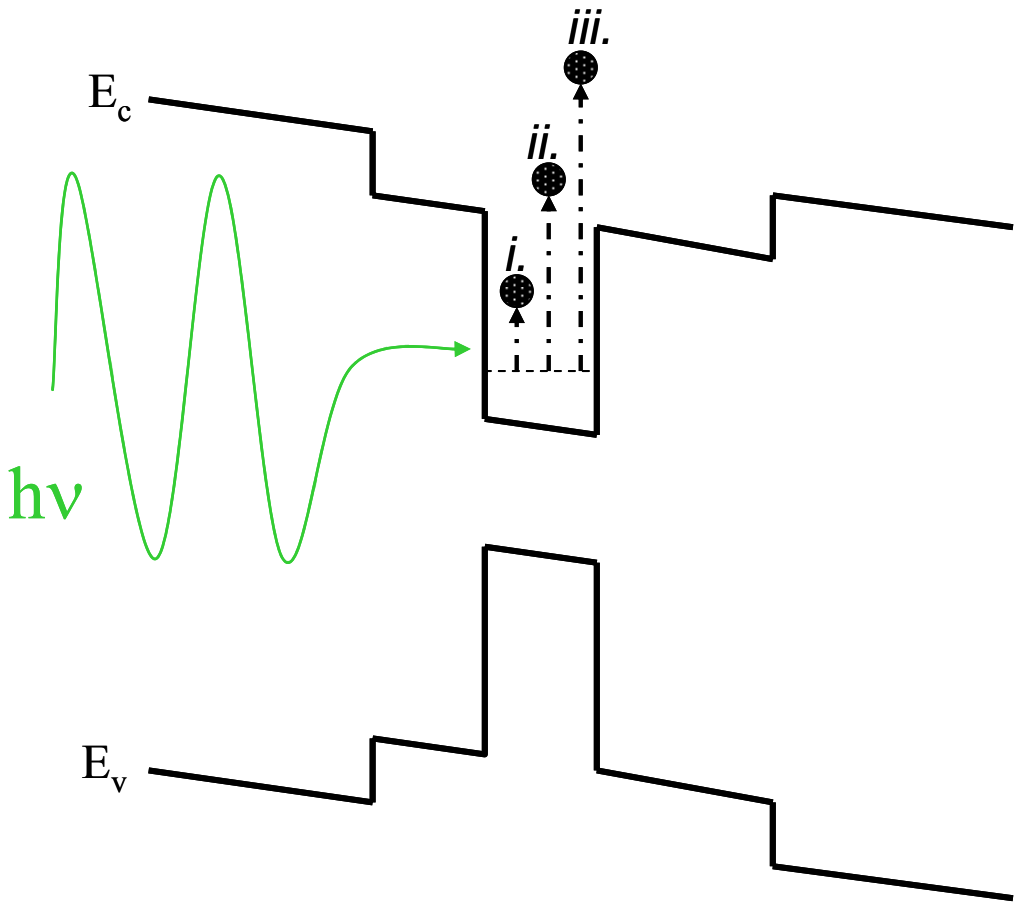

Figure 9. DWELL Energy Diagram Illustrating: (i.) Bound-to-Bound, (ii.) Bound-to-Quasi-bound, and (iii.) Bound-to-Continuum Transitions

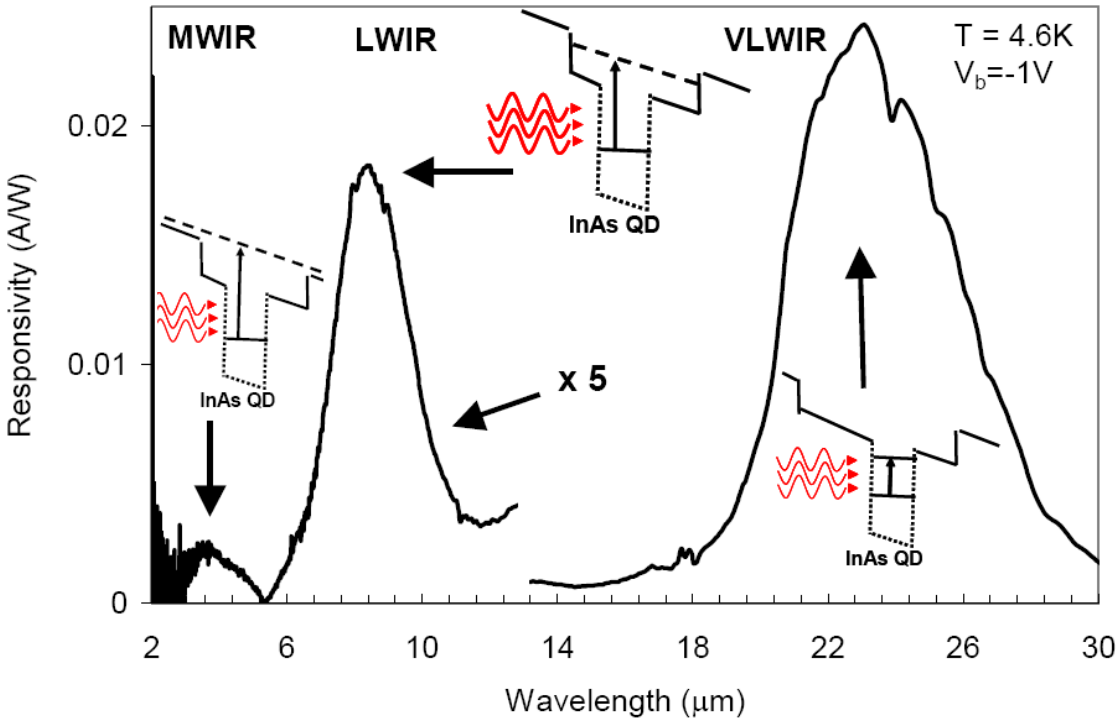

Figure 10. Measured Spectral Response of an InAs/InGaAs DWELL Demonstrating MWIR, LWIR and VLWIR Responses from Bound-to-Continuum, Bound-to-Quasi-bound, and Bound-to-Bound Transitions, respectively [9]

2.4 Quantum Dots-in-a-Well (DWELL) Infrared Focal Plane Array (FPA)

The focal plane array (FPA) evaluated and presented in this paper consists of 81,920 InAs/InGaAs quantum dots-in-a-well infrared photodetectors arranged in a 320x256 matrix. The structure of a single pixel device is shown in Figure 11. The single pixel device differs slightly from that of a conventional QDIP because the active region of QDs is embedded within an InGaAs quantum well [9]. This device has demonstrated two-color detection capability with response in the MWIR and LWIR regions. The performance characteristics of the DWELL FPA will be presented and analyzed in the unfiltered, MWIR, and LWIR bands.

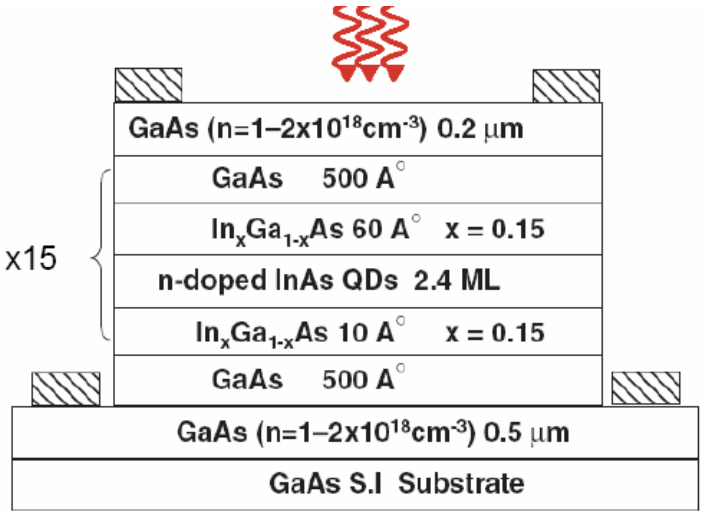

Figure 11. Diagram of the InAs/InGaAs DWELL [9]

2.5 Fabrication of the DWELL FPA

The sample used to create the DWELL FPA was grown by MBE using the already proven single pixel DWELL structure (see Figure 11). In the structure used to create the FPA, the active regions of each pixel consisted of fifteen layers of InAs quantum dots embedded in $In_{0.15}Ga_{0.85}As$ quantum wells. The pixels are essentially identical to the single pixel structure shown in Figure 11 above, except that the substrate and bottom GaAs layer are removed and the pixel is flipped by 180°. Following the growth process, the sample was processed into a 320x256 array of detectors using standard lithography (each pixel occupies an area of approximately $5.76x10^{-6}cm^2$, or $576\mu m^2$, and has a 25μm pitch). Processing included under bump metallization (UBM) and adding indium bumps at each detector location to facilitate device hybridization to a readout circuit, see Figure 12.

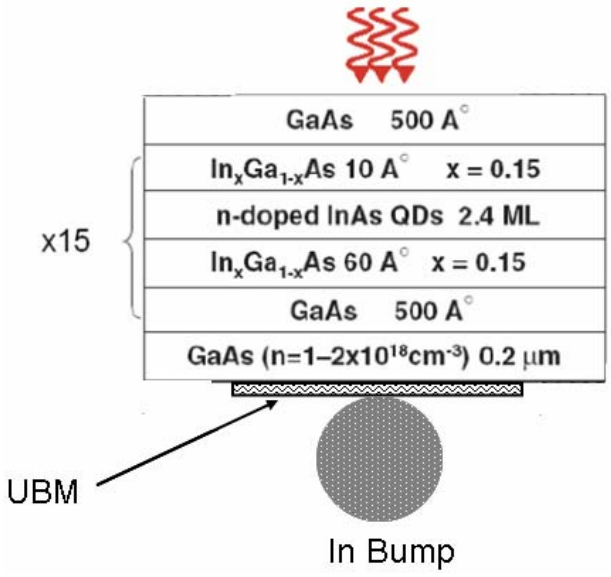

Figure 12. Schematic of a DWELL FPA Pixel

Figure 13 shows an SEM image of the DWELL FPA with indium bumps attached. The detector array was hybridized to a commercially available Indigo Systems Corporation ISC9705 readout integrated circuit (ROIC) by QmagiQ, Inc. to produce a usable FPA.

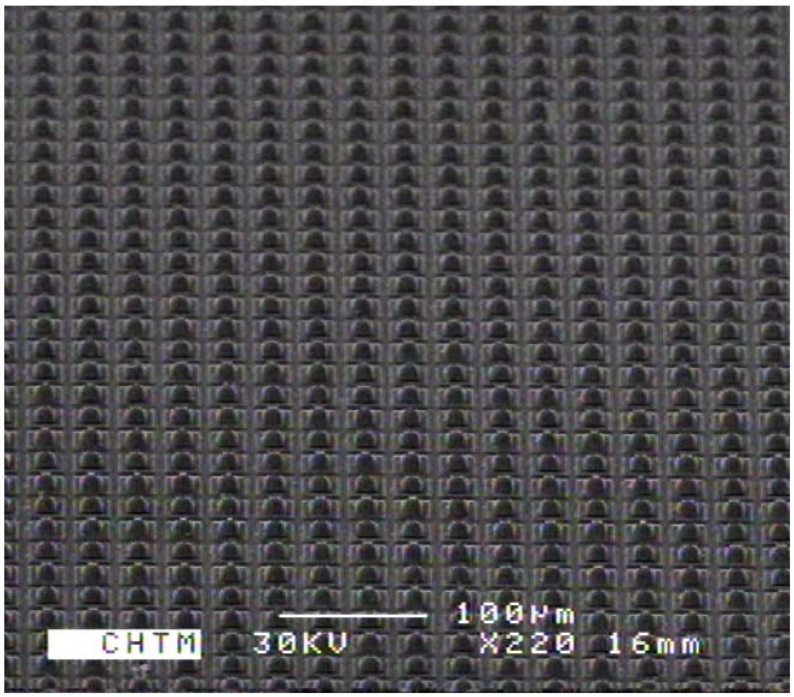

Figure 13. SEM Image of the DWELL FPA with In Bumps

Chapter 3

3 Materials and Methods

3.1 Indigo Systems Corporation ISC9705 Readout Integrated Circuit

The Indigo 9705 ROIC is a commercially available readout multiplexer chosen for hybridization because of its widespread use and affordability. The 9705, coupled with appropriate data acquisition hardware, provides the ability to measure individual pixel responses to capture an image. This ROIC design employs a common readout configuration known as direct injection to bias and receive signals from each pixel. The direct injection circuit achieves this by connecting each pixel in series with a PMOS transistor that is operated in weak inversion, and an integration capacitor, also referred to as the "well". This configuration is shown schematically in Figure 14. Under an applied bias, current flows through the detector and transistor, resulting in an accumulation of charge on each integration capacitor. The period of time over which charge is allowed to accumulate on the integration capacitor is referred to as the integration time (T_{int}). The integration time is user adjustable to accommodate a variety of operating conditions. During the readout process, the charge from each integration capacitor is transferred to a sample-and-hold (S/H) capacitor and is subsequently read by the data acquisition system via multiplexers within the ROIC. This measured voltage is an independent value for each pixel and is the signal digitized to create an image of the infrared scene that the FPA

viewed. This voltage also is used as a measure of detector performance.

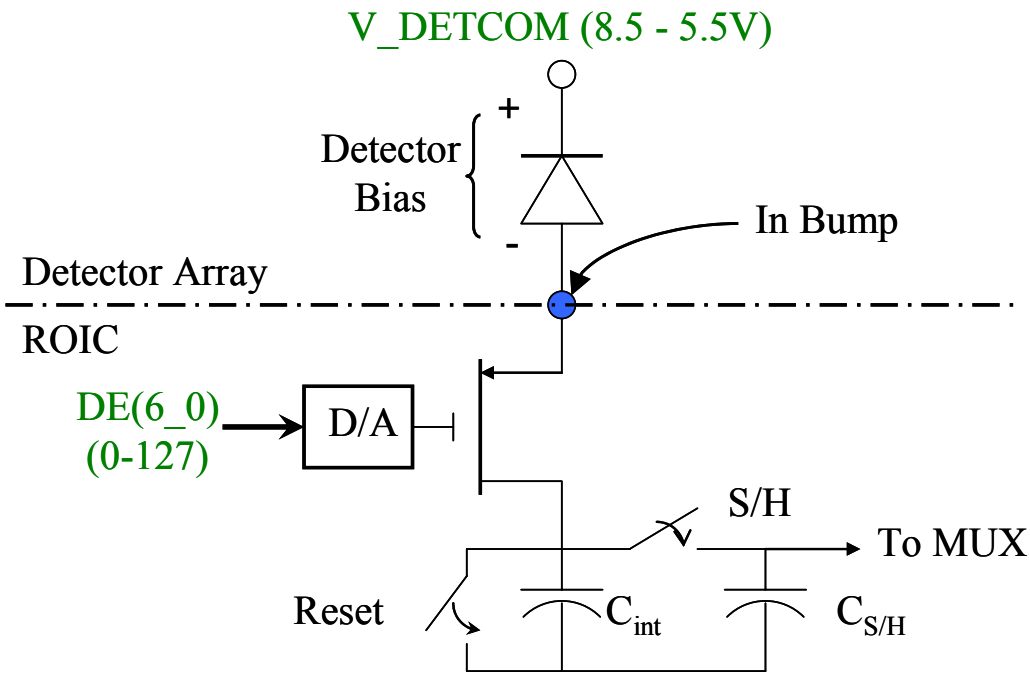

Figure 14. FPA Direct Injection Unit Cell

3.1.1 Calculating Detector Bias

The FPA camera system operator can manipulate the applied detector bias by adjusting two terms, V_{DETCOM}, the bias applied directly to the top terminal of each pixel, and *DE(6_0)*. The *DE(6_0)* parameter is a software adjustment value written to a digital-to-analog (D/A) within the ROIC that can contribute -0.1 to 0.5 volts of reverse bias voltage. The total voltage applied to the detector (V_{DETCOM}) can range from 8.5 to 5.5 volts. The 9705 implemented with the DWELL FPA is configured to apply a range of reverse bias voltages, but is capable of applying a weak forward bias voltage as well. Positive voltage

biases, as related to detector bias, represent reverse bias at each pixel. The maximum biases available with the 9705 ROIC are tabulated below in Table 2. *DE(6_0)* is fixed to provide approximately 0.5 volts of additional reverse bias voltage. The relationship between V_{DETCOM}, *DE(6_0)*, and detector bias voltage, V_{DB}, is defined in Equation 5,

Equation 5 $$V_{DB} = V_{DETCOM} - 5.5 + DE(6\_0).$$

Table 2. Indigo 9705 Bias Range

V_{DETCOM}	DE(6_0)	V_{DB} (reverse bias)
8.5 V	0.5 V	3.5 V
5.5 V	-0.1 V	-0.1 V

Calculating the actual detector voltage for a direct injection system is a non-trivial exercise due to the fact that the source-to-gate voltage on the PMOS transistors, therefore the bias on the detector, changes exponentially as a function of transistor drain current [21]. This change, referred to as ΔV_{SG}, moves a reverse biased detector towards a forward bias condition as the current is increased as shown by Equation 6,

Equation 6 $$V_{DB} = V_{DETCOM} - 5.5 + DE(6\_0) - \Delta V_{SG}.$$

This effect is noted by Indigo specifications to be approximately 44 to 55 mV per decade of current increase from 20 pA to 1 nA.

To estimate the magnitude of this bias change, Equation 7 [21],

Equation 7 $$I_D = K\frac{1}{m}(nkT)^2 \exp\left[\frac{1}{nkT}(V_{GS} - V_T - nkT)\right]\left\{1 - \exp\left[-\frac{m}{nkT}V_D\right]\right\},$$

was evaluated over a range of currents from 10 pA to 10 nA at three different temperatures. The product of this evaluation, presented in Figure 15, and the information in Table 3 confirm that the quantities reported by Indigo are of the right order of magnitude. The results demonstrate that for expected pixel current values (nanoamps) and temperatures (< 100K) the change in detector bias attributed to increasing detector current is negligible as compared to the range of biases that can be applied with the 9705 ROIC.

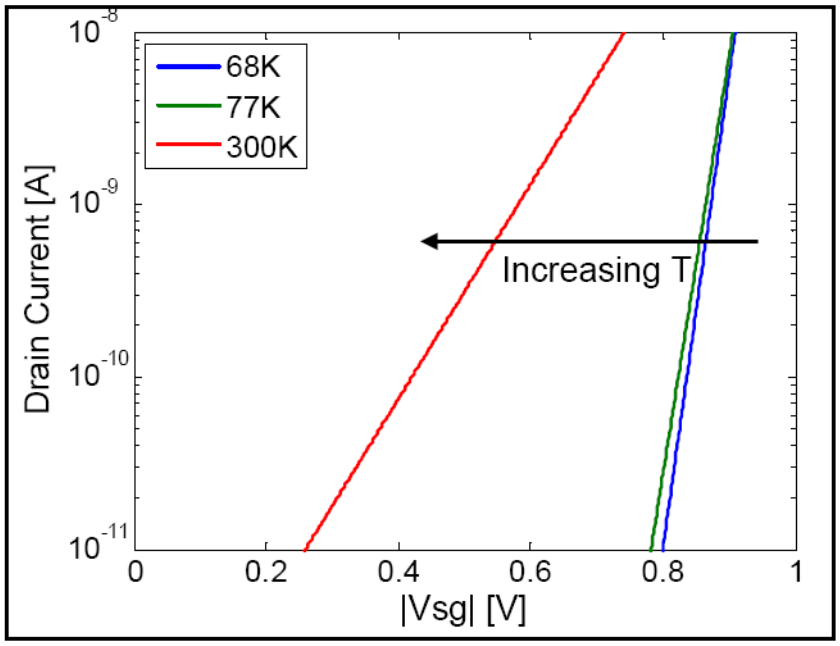

Figure 15. PMOS Source-to-Gate Voltage Versus Drain Current

Table 3. Estimate of ΔV_{SG} Values

T [K]	***V_{SG} (10pA) [V]***	***V_{SG} (1000pA) [V]***	***ΔV_{SG} per decade [V]***
68	0.8	0.908	0.036
77	0.782	0.905	0.041
300	0.26	0.741	0.16

3.1.2 ROIC Gain Setting

The Indigo 9705 ROIC provides the user with four settings of an adjustable conversion gain, C_G. This conversion gain is a feature of the ROIC that changes the unit cell well voltage contribution of each collected electron. The conversion gain is adjusted by changing a two-bit binary value in SE-IR CamIRa™ software used in the data acquisition system (discussed in section 3.2). This affords the user flexibility in a variety of operating conditions, however this also changes the signal-to-noise ratio of the FPA; as the conversion gain is increased, noise is also increased. A laboratory experiment was conducted to determine the optimum setting of C_G for the DWELL FPA analysis to follow (see Table 4). The results indicate that a C_G setting of 10 produces the best SNR. The remainder of the DWELL FPA analysis was conducted at a C_G setting of 10.

Table 4. Conversion Gain Experiment Results

C_G	T_{int} [ms]	V_n [V_{rms}]	V_o [V]	E_q [photons/sec-cm^2]	SNR
00	1.971 1.971	4.017E-04 4.054E-04	2.576 2.581	7.81E+14 1.16E+15	11.221
01	1.971 1.971	5.164E-04 5.087E-04	2.570 2.578	7.81E+14 1.16E+15	14.846
10	1.971 1.971	7.407E-04 7.426E-04	3.158 3.169	7.81E+14 1.16E+15	**14.928**
11	1.971 1.971	1.461E-03 1.454E-03	4.337 4.351	7.81E+14 1.16E+15	9.124

3.2 SE-IR CamIRa™ Data Acquisition Setup

The data acquisition hardware used to analyze the DWELL FPA was a commercially available CamIRa™ system from SE-IR Corporation. This system operated the ROIC and captured experimental data. A block diagram of the CamIRa™ setup is shown below in Figure 16.

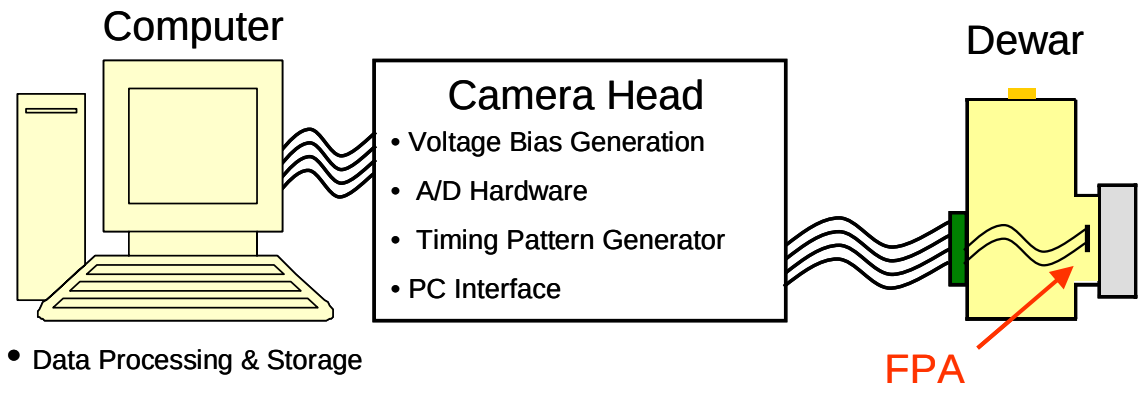

Figure 16. Block Diagram of the CamIRa™ System

3.3 DWELL FPA Performance Measurements

After hybridizing to the ROIC, performance measurements of a FPA becomes more complicated when compared with the characterization of a single pixel detector. Previous experiments attempted to measure device current in series with the V_{DETCOM} terminal (under various bias and irradiance conditions), making the assumption that dividing this current by 81,920 would yield average individual pixel current. This method was problematic because measured currents did not represent the performance of the array. The effects of bad pixels (i.e., pixels that were either shorted out or open) could not be isolated as well as other current sinks in the FPA that changed the current sourced to the detector array. The method selected for measuring FPA performance used output voltage captured at each pixel by the CamIRa™ system as the signal from which performance measures were determined. Careful attention to the signals was necessary to ensure that recorded voltages did not include any gains associated with the system A/D stages. Voltages used in performance measurements did include gain (C_G) and noise contributions associated with the ROIC, however.

This is a viable method of characterization as the ROIC is an integral part of the FPA. Any enhancements or degradation to device performance should be included because any FPA camera system is incomplete without a ROIC. All performance measurements were carried out at a FPA temperature of 77K, unless noted otherwise.

3.3.1 FPA Temporal Noise Measurement

Given that the CamIRa™ system is used as a platform for operating FPA cameras, measurements were made from collected image frames consisting of a matrix of 320x256

independent analog-to-digital count (ADC) values. The total number of frames captured for a given measurement represents the number of values that are used to determine the temporal RMS noise voltage level (about the mean value at each pixel). The average temporal noise of the entire array would therefore be the average of all 81,920 RMS values. To determine the required number of frames necessary to obtain a representative RMS noise level, an experiment was performed in which the FPA average RMS noise was computed for an increasing number of collected image frames. The results of this test (shown in Figure 17) demonstrated that the array RMS noise level has converged after approximately 30 frames. From this experiment, it was decided that all following output voltage measurements would be made with 100 collected image frames.

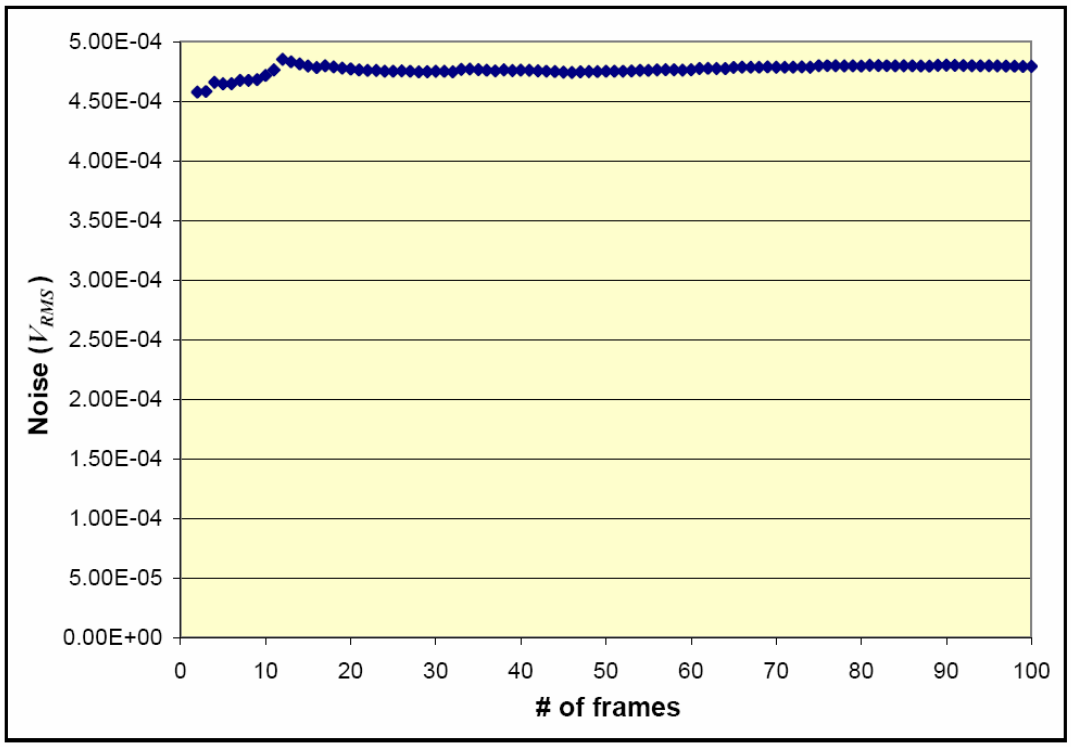

Figure 17. FPA Temporal RMS Noise Voltage versus Number of Frames

3.3.1.1 FPA Camera System Noise Measurement

Before collecting FPA performance measures, it was important to determine noise voltage levels associated with the SE-IR A/D circuitry. To obtain this noise parameter, a clean DC voltage source having a nominal noise voltage of $2.5\mu V_{RMS}$ was injected into the camera head A/D input port where FPA output is normally connected. Just as FPA voltages were processed by the data acquisition hardware, this known, low-noise reference signal was digitized to determine the noise contributions of the A/D hardware. The results of this experiment (see Figure 18) showed that the system noise level was roughly $93\mu V_{RMS}$. This measured noise is not attributed to the FPA or ROIC; therefore, it was subtracted (in quadrature) from all noise measurements, as shown by Equation 8,

Equation 8

$$V_n = \sqrt{V_{nTotal}{}^2 - (93.1x10^{-6})^2} \ .$$

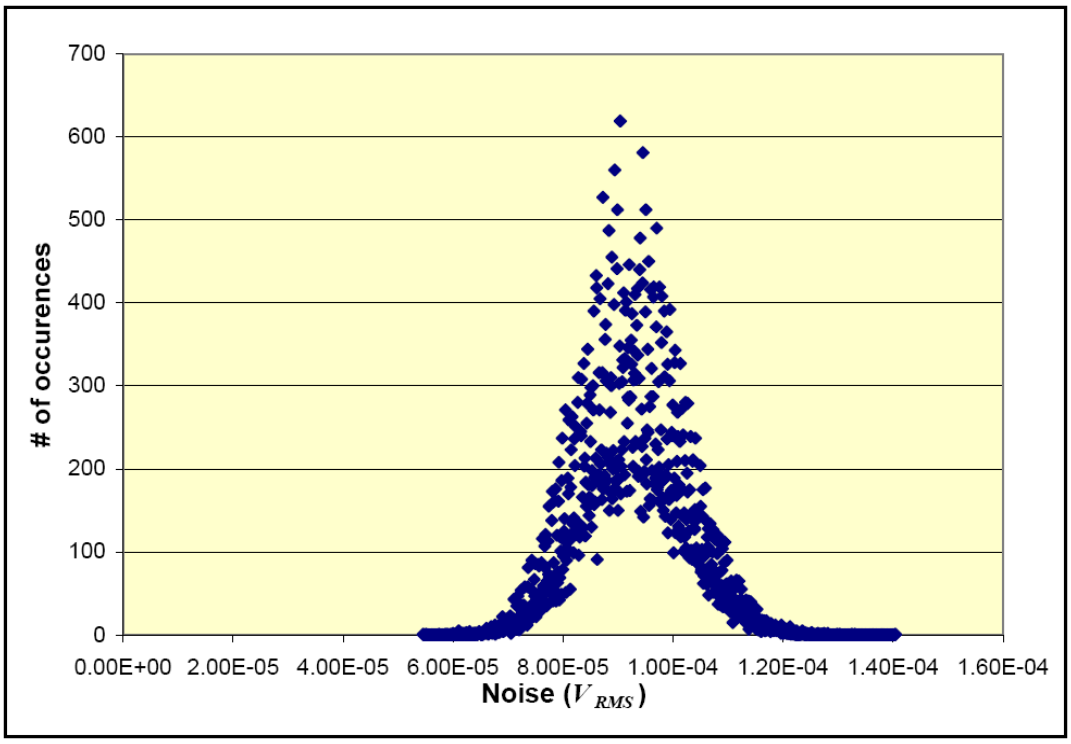

Figure 18. SE-IR CamIRa™ System Noise Voltage

3.3.1.2 Total Noise Measurement

FPA noise was measured as a function of irradiance at four detector biases (V_{DB} ~0.5, 0.75, 1.0, and 1.1 volts), see Figure 19. Photon irradiance was provided via a calibrated blackbody source operated over a range of temperatures from 25C up to 255C (irradiance calculations discussed in section 3.4.3). Readout integration times at each bias used throughout the study are shown in Table 5.

Table 5. FPA Readout Integration Times

V_{DB}	*Integration Time (ms)*
0.5	2.365
0.75	1.014
1.0	0.225
1.1	0.169

The total FPA noise is described by Equation 9,

Equation 9

$$V_n^2 = V_{nDetector}^2 + V_{n\,\mathrm{Re}adout}^2 .$$

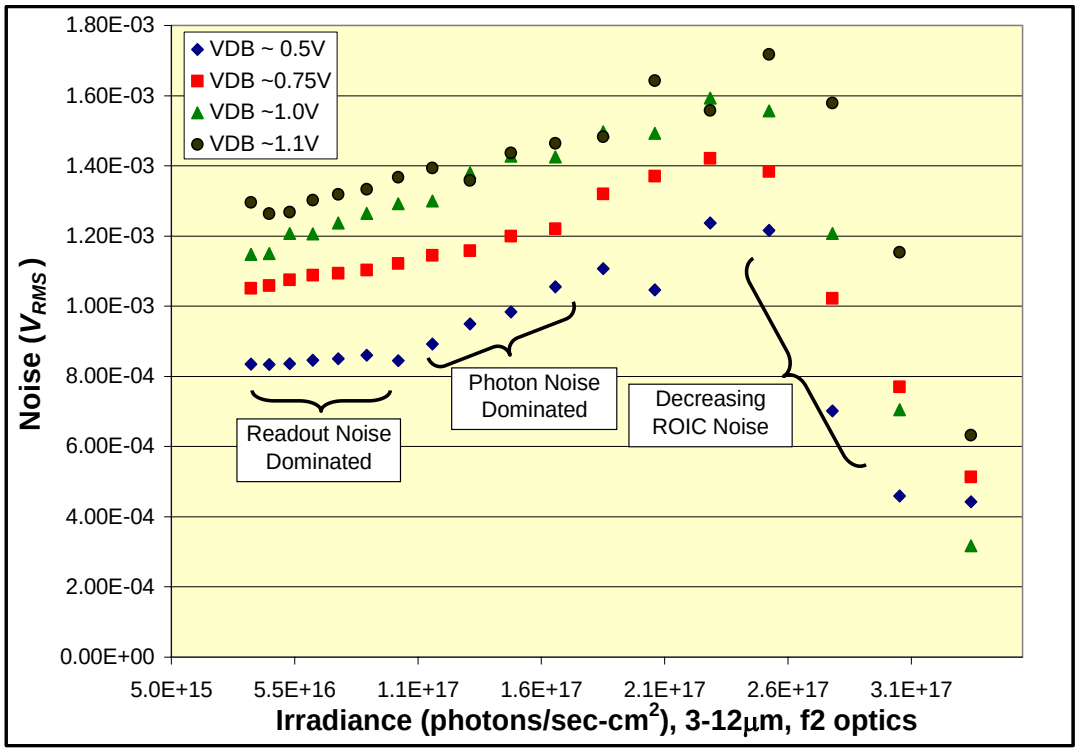

Figure 19. FPA Noise versus Photon Irradiance at 77K

At a detector bias of V_{DB} ~0.5V, the DWELL FPA displayed photon noise limited conditions at low irradiances up to ~6 x 10^{15} photons/sec-cm^2, where the dominant noise

was due to readout noise from the ROIC. Beyond ~6 x 10^{15} photons/sec-cm^2 the FPA was background noise limited (BLIP) until the ROIC integration capacitors were nearly full, at which point the readout noise was observed to fall off. Under BLIP conditions the dominant contributor to detector noise was generation-recombination noise caused by photogenerated carriers from the incident flux of photons. This contribution to noise is proportional to the square-root of the number of incident photons and is the cause of the increase in total FPA noise with increased irradiance (after readout noise is no longer the dominant noise source and until the integration capacitors start to fill), shown by Equation 10,

Equation 10

$$V_{nPhoton} = C_G G \sqrt{2\eta E_q A_d T_{\text{int}}} \ ,$$

where C_G is conversion gain (volts per electron), G is photoconductive gain, η is detector quantum efficiency (electrons per photon), E_q is photon irradiance [photons/sec-cm^2], A_d is detector area [cm^2], and T_{int} is integration time [s].

At increased detector biases (~0.75, 1.0, and 1.1V), the DWELL FPA did not exhibit photon noise limited conditions at low irradiances and was background noise limited until the integration capacitors were nearly full, when the readout noise began to decline.

3.3.1.3 Sources of Readout Noise

At low photon irradiances, ROIC readout noise is the dominant contributor to FPA noise. Readout noise comes from multiple sources (see Equation 11), of which, the major

source is reset noise associated with the ROIC [20],

Equation 11

$$V_{nreadout}^2 = V_{nreset}^2 + V_{nCG}^2 + V_{nJohnson}^2 .$$

Reset noise is a Johnson noise resulting from the movement of charge through the reset transistor and causes uncertainty in the reset voltage stored in the integration capacitors. As the stored voltage in the well approaches full well, the reset noise contributed to the readout noise begins to drop. This effect can be used to estimate the reset noise of the DWELL FPA by using Equation 12,

Equation 12

$$V_{nreset} = \sqrt{V_{nreadout}^2 - V_{nfullwell}^2} .$$

From Figure 19, looking at the lowest noise case at a detector bias of ~0.5V, $V_{nreadout}$ is approximately 842μV and $V_{nfullwell}$ is approximately 450μV, resulting in a reset noise of approximately 712μV.

3.3.2 Spatial Noise Measurements

The spatial noise of a FPA is a noise source introduced by variations in pixel responses to a uniform scene. These variations cause distortions in the images recorded from the FPA. Spatial noise is determined by capturing an image of a uniform scene supplied by a calibrated black body that fills the FPA field of view. This measurement depicts the uniformity of performance across the detector array and is a strong function of array non-

uniformity correction, or NUC. NUC provides a correction of each individual pixel response such that the image of a uniform scene will exhibit consistent response across the entire array. As an example, two pixels with different responses at two scene temperatures (such as pixel A and pixel B depicted in Figure 20) can be adjusted such that the responses appear similar. Spatial noise does not have a strong influence over the detector array average performance since, in general, only a small portion of the array pixels receive significant correction. Spatial noise requires correction so that clear images can be obtained. Images captured by the DWELL FPA with a calibrated black body source with and without an applied NUC are shown in Figure 21. DWELL FPA spatial noise was calculated as 101.75mV without NUC applied and 3.58mV with NUC.

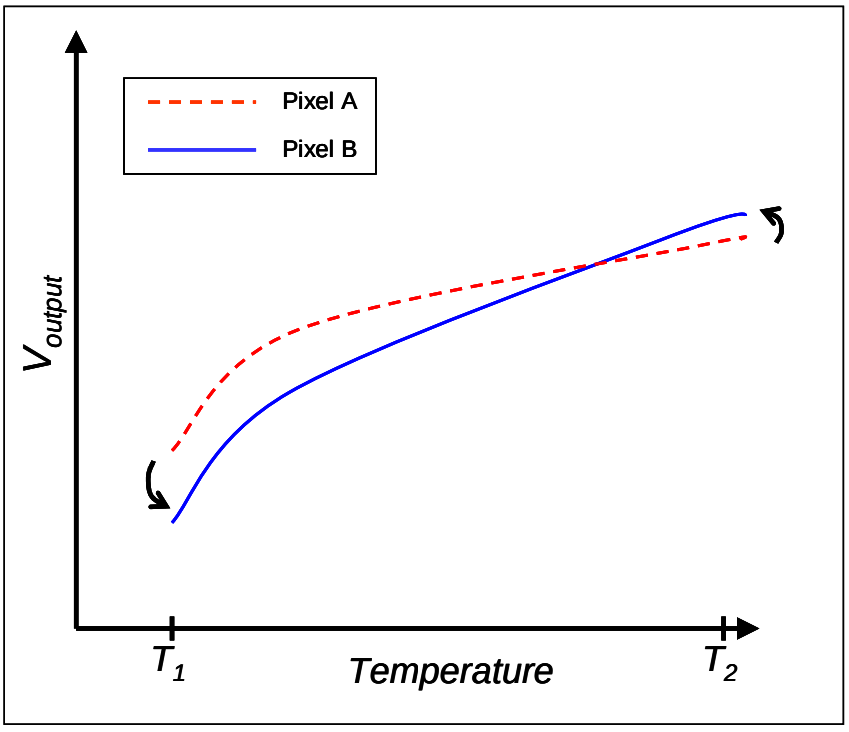

Figure 20. Non-Uniformity Correction Example

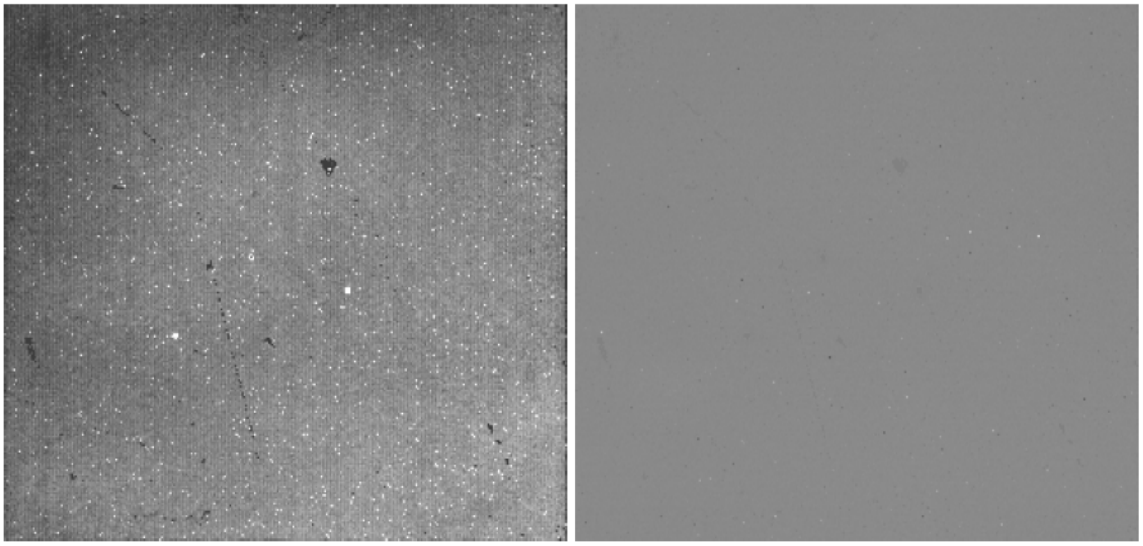

Figure 21. Images Captured Without and With NUC (left and right, respectively)

3.4 FPA Spectral Response Measurements

First generation IR detector systems consisted of a scanning linear array of devices used to create imaging systems. Advances in detector technology and the invention of charge coupled devices (CCDs) led to the development of second generation devices. Second generation systems have more elements (typically three orders of magnitude, for a total of $>10^6$) on the focal plane than first generation devices, and the detector elements are arranged in a two-dimensional array. These arrays are electronically scanned by readout circuits integrated with the array. Third generation detectors are similar to second generation devices but offer enhanced capabilities including: higher number of pixels, higher frame rates, and better thermal resolution [17]. In addition, one of the main drivers in the design of third generation infrared photodetectors is to create devices with multi-color functionality. In the course of collecting data from the DWELL FPA, test equipment was acquired to measure the response of the array to tunable monochromatic

light to begin to develop an understanding of the spectral response of our hybridized devices and how they may address the multi-color requirement of third generation systems. In most cases, single pixel spectral response data are collected and are assumed to apply to an entire array of pixels. This, however, may not be the case due to a variety of reasons including device processing and hybridization to a ROIC. In the testing of the DWELL FPA presented in this report the spectral response of the array was measured by introducing adjustable monochromatic light spanning the wavelength band of 3-12μm .

3.4.1 FPA Spectral Response Test Setup

To conduct spectral response measurements a PIActon Spectra Pro 2150i monochromator was used as a monochromatic light source (spectrograph). An Oriel 6363 IR emitter mounted in a light source provided gray body radiation that passed through appropriately selected long-wave pass filters (to eliminate 2^{nd} order light effects). The monochromator was equipped with a dual-grating turret (one grating blazed at 4μm, the other at 8μm) that provided the user tunable monochromatic light. Figure 22 shows a diagram of the test setup used. Table 6 lists the long-wave pass filters used in the test apparatus and Table 7 lists the monochromator grating filter optimum operating ranges.

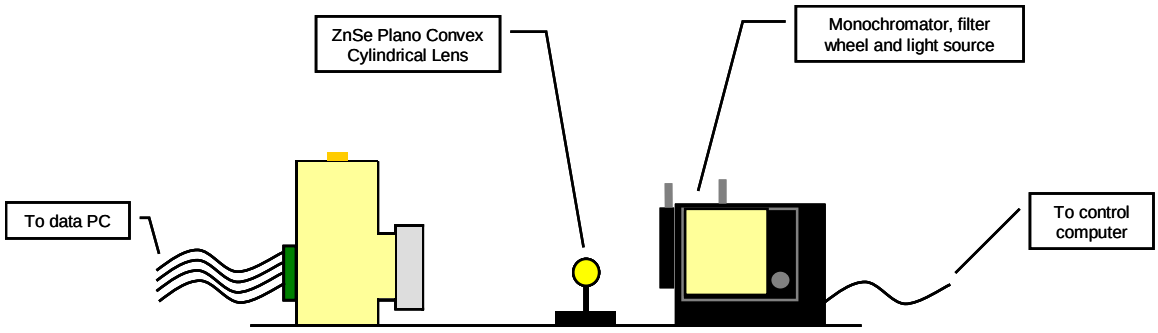

Figure 22. FPA Spectral Response Measurement Setup

Table 6. Optimum Operating Range of Long-wave Pass Filters [from Spectrogon, Inc].

Filter	***Optimum Operating Range [nm]***
1	2703 – 5258
2	5525 – 11876
3	8143 – 24938

Table 7. Optimum Operating Range of Monochromator Gratings [from PIActon, Inc].

Grating	***Optimum Operating Range [μm]***
1 (150g/mm, blazed at 4μm)	2.6 – 6
2 (75g/mm, blazed at 8μm)	5.3 – 12

To address the manufacturers' (Spectrogon and PIActon for the filters and gratings, respectively) listed optimum operating ranges, the spectral response measurement was designed to operate within these ranges. Figure 23 and Figure 24 show the usage of the monochromator gratings and long-wave pass filters.

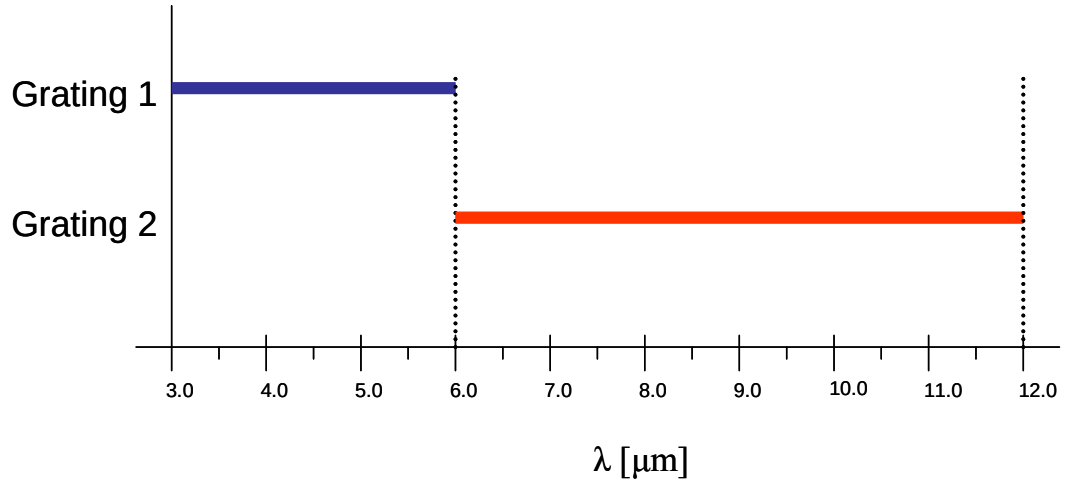

Figure 23. Usage of Monochromator Gratings in FPA Spectral Response Measurements.

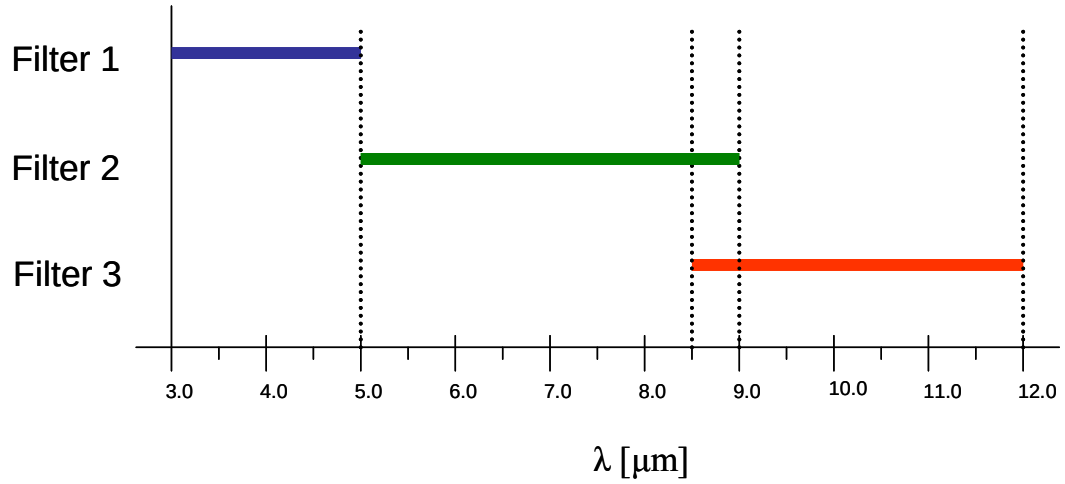

Figure 24. Usage of Long-wave Pass Filters in FPA Spectral Response Measurements.

With this monochromator test setup in place, the spectral response of the DWELL FPA was measured at the four detector biases of ~0.5, 0.75, 1.0, and 1.1V by scanning the light incident on the array from 3-12μm in 100nm steps.

3.4.2 FPA Spectral Response Results

Five trials of spectral response measurements were conducted at each bias following the test method described in section 3.5.1. Two representative normalized response curves from these tests are shown in Figure 25 and Figure 26. Notice that there is some overestimation of response near 3.5μm. This is due to the low transmission of photons through the monochromator grating and filter (~40%) that comes into consideration by Equation 13,

Equation 13

$$R(\lambda) = \frac{V_{output}}{\varepsilon(\lambda) M(\lambda, T) \tau(\lambda)}$$

where $R(\lambda)$ is the FPA response at a given wavelength, V_{output} is FPA output voltage [V], $\varepsilon(\lambda)$ is the IR emitter emissivity (provided by the manufacturer), $M(\lambda,T)$ is the IR emitter spectral exitance, and $\tau(\lambda)$ is transmission of gratings and filters. Equation 13 was used to account for the spectral dependence of the output of the Oriel 6363 IR emitter gray body source.

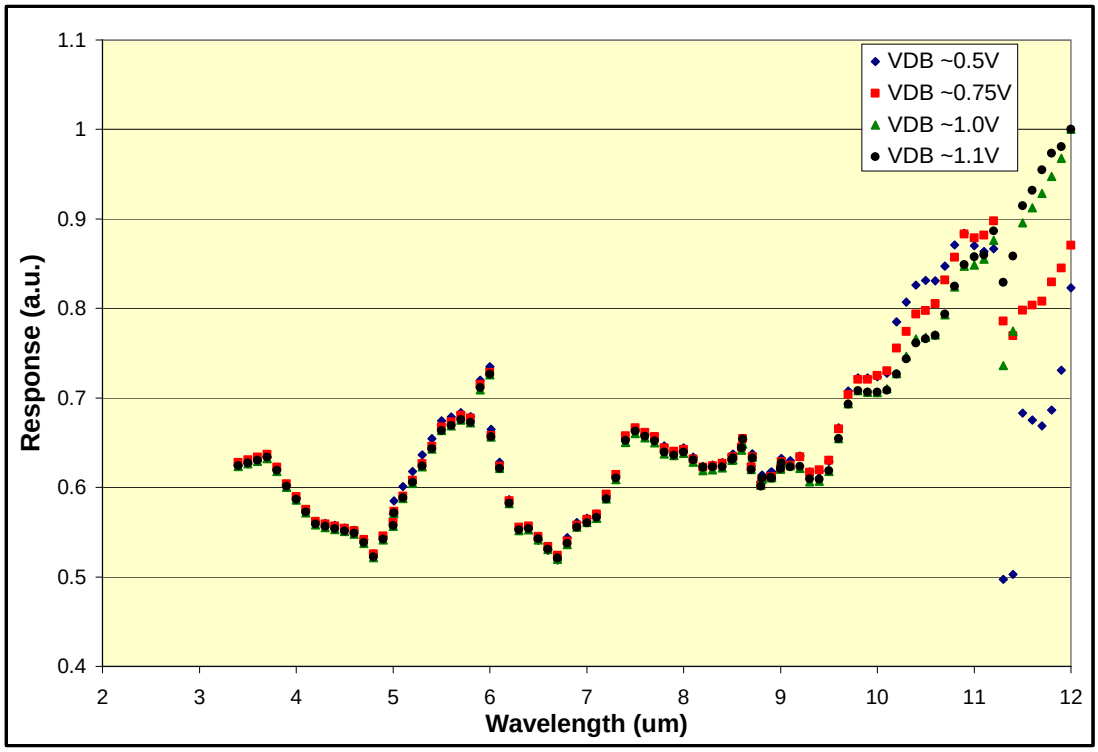

Figure 25. FPA Response versus Wavelength (Trial 1).

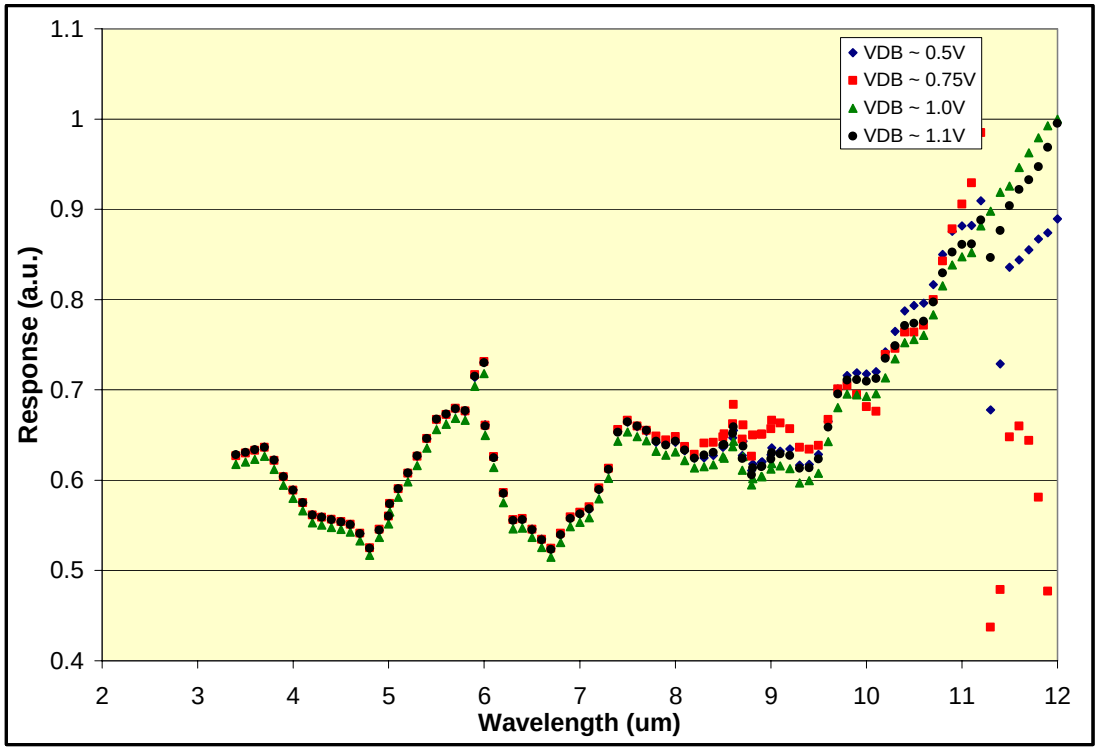

Figure 26. FPA Response versus Wavelength (Trial 2).

Peak responses were noted at ~6μm and at ~7.5μm, with an increase in response from 9.5 to 12μm. Again there appears to be some overestimation in response due to decreasing transmission (τ) of the monochromator grating and long-wave pass filter at wavelengths greater than 10μm. Notice that it does appear that stronger LWIR response is seen as the detector bias is increased, most notably between 11-12μm. The spectral response measured in this experiment does resemble the spectral response of a typical single pixel DWELL detector at a reverse bias of 1.0V shown in Figure 27. The single pixel device exhibited enhanced LWIR response at increased detector bias as a result of increased tunneling probability for carriers excited in bound-to-bound and bound-to-quasi-bound transitions. Comparing these first spectral response measurements of the entire DWELL FPA to those of the typical single pixel DWELL, it does not appear that there is as much spectral tunability with the detector biases available from the 9705 ROIC. The spectral response of the DWELL FPA was collected, showing clear two-color response. With this information, the broadband and two-color figures of merit could be determined.

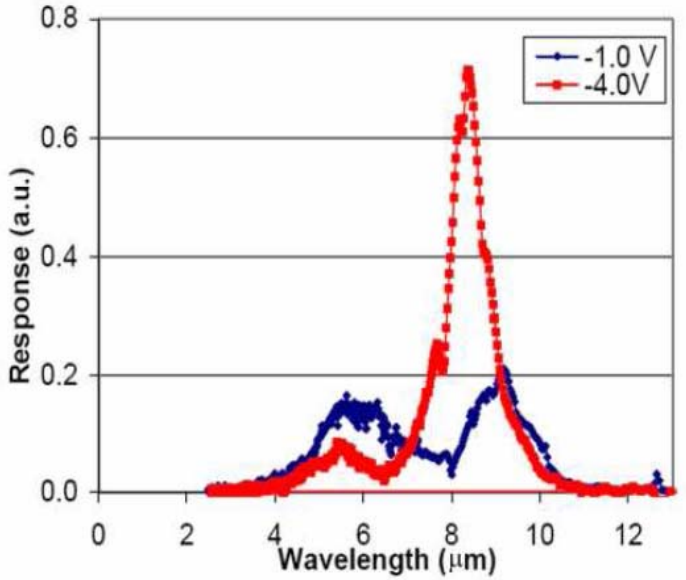

Figure 27. Spectral Response of a Typical DWELL Detector.

Chapter 4

4 Broadband Figures of Merit

Prior to measuring the two-color performance of the DWELL FPA, the unfiltered (not using optics, or "broadband") response of the FPA was measured at four detector bias levels (V_{DB} ~0.5, 0.75, 1.0 and 1.1V). Several detector figures of merit were calculated by measuring mean FPA output and noise versus irradiance. Irradiance was provided by a calibrated black body source operated over a wide temperature range. Irradiance values (E_q [photons/sec-cm^2] and E_e [Watts/cm^2]) at the FPA were assumed to be uniform across the array and were calculated using Equations 14 through 17 [4]. The output of the DWELL FPA displayed a fairly linear response as a function of irradiance (as shown in Figure 28) until the ROIC integration capacitors were full at approximately 5.25 volts. Once this output voltage was reached, no further FPA response could be measured,

Equation 14

$$E_q = \frac{\pi L_q}{4(f\#)^2 + 1}$$

where L_q is photon radiance [photons/cm^2-sec-sr-μm],

Equation 15

$$L_q = \frac{2c}{\lambda^4\left(\exp\left(hc/\lambda kT\right) - 1\right)}$$

where h is Planck's constant [6.626 x 10^{-34}J-s], c is the speed of light [2.998 x 10^8 m/s], k is Boltzmann's constant [1.381 x 10^{-23} J/K], T is temperature [K],

Equation 16

$$E_e = \frac{\pi L_e}{4(f\#)^2 + 1}$$

L_e is photon radiance [Watts/(cm^2-sr-μm)],

Equation 17

$$L_e = \frac{2hc^2}{\lambda^5\left(\exp\left(hc/\lambda kT\right) - 1\right)}.$$

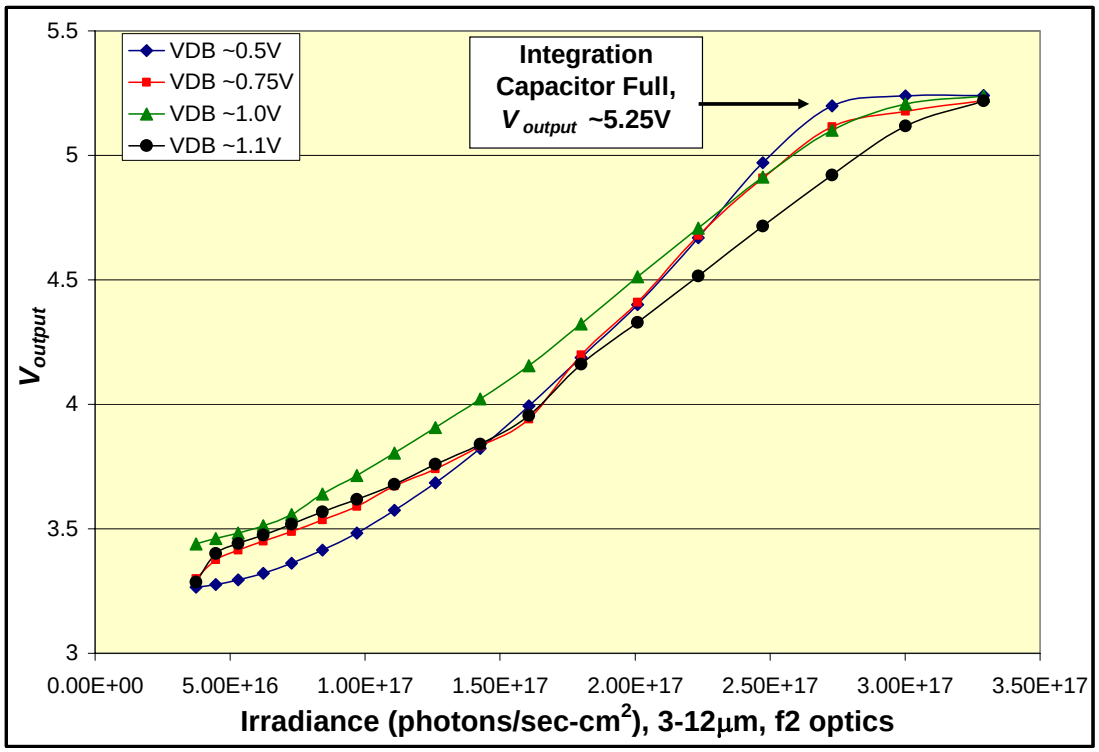

Figure 28. Output Voltage versus Irradiance for the DWELL FPA at 77K

When the detector array is operated in a photon shot noise dominant regime, the voltage output of DWELL FPA (V_{output}) along with the photon noise voltage (in Equation 10) can be utilized to calculate the conversion gain product, $C_G G$. Squaring Equation 10 yields noise variance which can be used to solve for $\eta G E_q A_d T_{int}$. Next, this quantity can be substituted in Equation 18,

Equation 18

$$V_{output} = C_G\left(\eta G E_q A_d T_{\text{int}} + \frac{I_{dark} T_{\text{int}}}{q}\right)$$

where C_G is conversion gain, η is detector quantum efficiency [electrons per photon], G is photoconductive gain, E_q is photon irradiance [photons/sec-cm^2], A_d is detector area [cm^2], T_{int} is integration time [sec], I_{dark} is detector dark current [amps] and q is electron charge [1.6 x 10^{-19} Coulombs]. The slope of the resulting equation given by Equation 19,

Equation 19

$$V_{nPhoton}^2 = 2C_G G\left(V_{output}\right) - 2C_G^2 G\frac{I_{dark} T_{\text{int}}}{q}$$

corresponds to the $C_G G$ product. This method was used to generate Figure 29 and provide an estimate of the conversion-gain product at the four test biases. The DWELL array revealed the anticipated trend of higher $C_G G$ at higher biases (from the contribution of G) [3]. Estimated $C_G G$ product values for the four detector test biases are shown in Table 8.

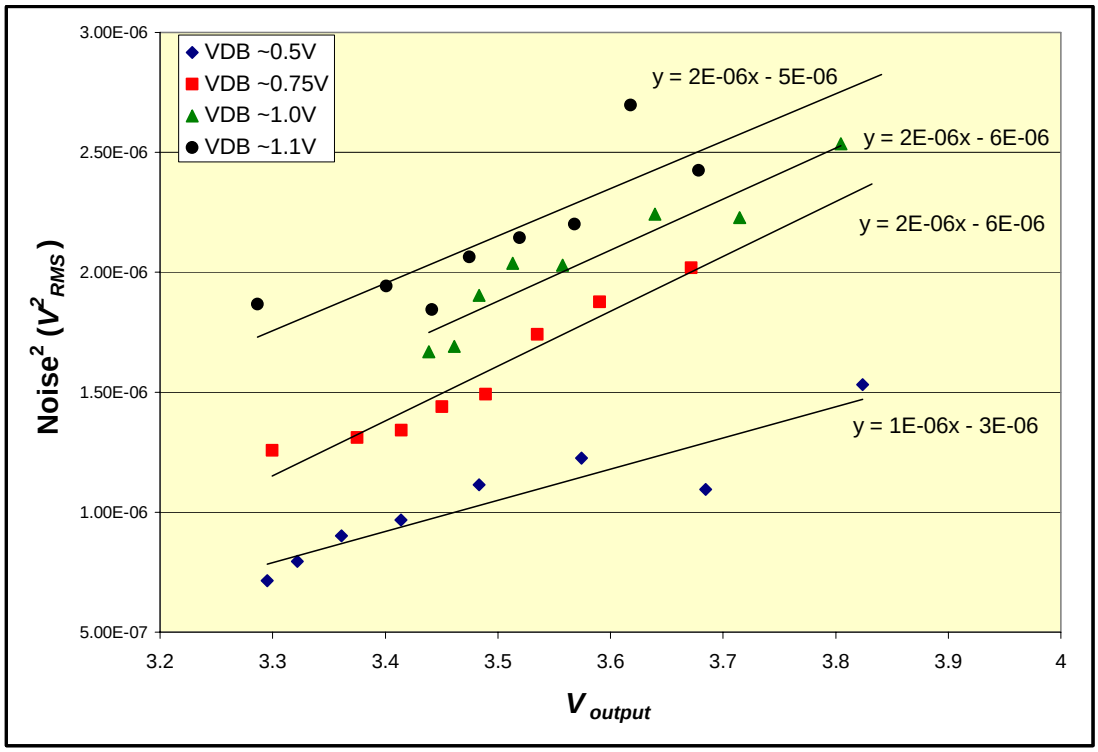

Figure 29. Detector Noise Variance versus Output at 77K

Table 8. C_GG Conversion Gain Product Estimates at 77K

V_{DETCOM}	C_GG [V/electron]
5.5	1.30×10^{-6}
5.75	2.29×10^{-6}
6.0	2.13×10^{-6}
6.1	1.98×10^{-6}

4.1 Responsivity

Responsivity is a quantity that represents detector output per unit of radiant input. A high responsivity is desired for this quantity, as responsivity is proportional to the detector quantum efficiency (*QE*). In the case of the DWELL FPA, responsivity is proportional to the QE, photoconductive gain (*G*), and conversion gain (C_G) product. Device

responsivity was measured at four detector biases (V_{DB} ~0.5, 0.75, 1.0, and 1.1 volts) by measuring FPA output voltage versus irradiance (Figure 28). Equations 20 and 21 were used to calculate peak responsivities,

Equation 20

$$R_v\left[\frac{V}{photon}\right] = \frac{V_{output}}{\sum_{3\,\mu m}^{12\,\mu m} R_n(\lambda) E_q(\lambda, T)\tau_{win} d\lambda} \text{ and}$$

Equation 21

$$R_v\left[\frac{V}{W}\right] = \frac{V_{output}}{\sum_{3\,\mu m}^{12\,\mu m} R_n(\lambda) E_e(\lambda, T)\tau_{win} d\lambda}$$

where V_{output} is FPA output voltage [V], R_n is normalized spectral response, E_q is photon irradiance [photons/sec-cm^2], E_e is irradiance [Watts/cm^2], and $d\lambda$ is wavelength scanning step size from spectral response data [100nm].

To complete the peak responsivity calculations the collected spectral response data (section 3.4.2) was used. The responsivity results are tabulated in Table 9.

Table 9. Responsivity Values at 77K

V_{DB}	R_v (V/photon)	R_v (V/W)
0.5	5.114E-10	4.316E+07
0.75	1.243E-09	4.701E+07
1.0	3.806E-09	3.163E+07
1.1	8.325E-09	6.048E+07

4.2 Noise Equivalent Power

Noise equivalent power (NEP) is a parameter defined as the required optical power

incident on a photodetector that produces a signal-to-noise ratio equal to 1. This represents the minimum amount of optical input power that must be exceeded for detection to occur. A low value of NEP is an indicator of good detector performance, indicating a small amount of optical input is detectable. DWELL FPA NEP was calculated using calculated responsivity and Equation 22 [4],

Equation 22

$$NEP = \frac{V_n}{R_v}$$

where V_n is recorded noise voltage [V_{RMS}] and R_v is voltage responsivity [V/W]. NEP is plotted against irradiance in Figure 30 below. Minimum NEP values at each detector test bias are shown in Table 10.

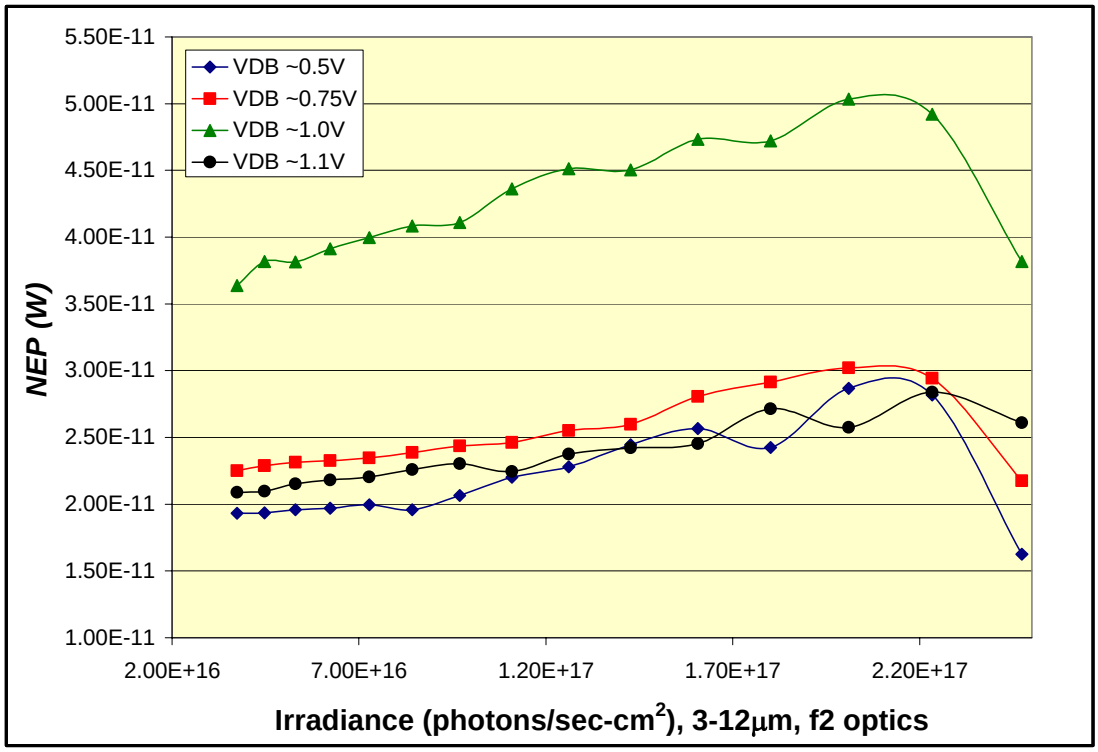

Figure 30. NEP versus Irradiance at 77K

Table 10. Minimum Recorded NEP Results at 77K

V_{DB}	NEP (W)
0.5	1.627E-11
0.75	2.174E-11
1.0	3.637E-11
1.1	2.089E-11

4.3 Noise Equivalent Irradiance

Noise equivalent irradiance (NEI), is defined as the number of photons per unit area incident upon a photodetector that produce a signal-to-noise ratio equal to 1 (NEI is a units change from NEP). NEI was calculated with Equation 23,

Equation 23

$$NEI = \frac{V_n}{R_v A_d}$$

where V_n is recorded noise voltage [V_{RMS}], R_v is voltage responsivity [V/photon] and A_d is detector area [cm^2]. It should be noted that there is another definition of NEI that defined as the irradiance at an f1 input, rather than at the detector. Figure 31 shows NEI plotted versus detector irradiance for the four test biases. Minimum NEI values are listed in Table 11.

Table 11. Minimum Recorded NEI Results at 77K

V_{DB}	$NEI\ (photons/cm^2)$
0.5	2.829E+11
0.75	1.478E+11
1.0	5.242E+10
1.1	2.635E+10

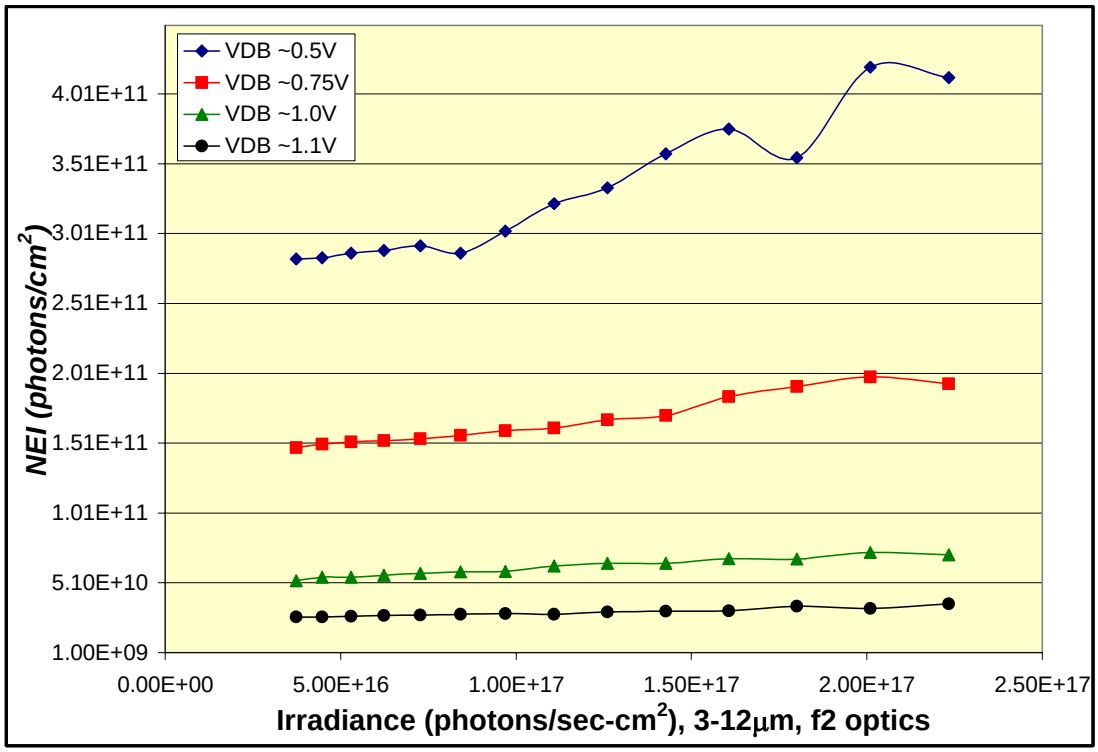

Figure 31. NEI versus Irradiance at 77K

4.4 Detectivity

The detectivity, denoted by D*, of a photodetector (units of cm-(Hz)$^{1/2}$/W) is inversely proportional to the detector NEP. High detectivity is a desired trait because it implies that small amounts of optical power can be detected. DWELL FPA detectivity was calculated using the NEP calculation results and Equation 24 [24] and Equation 25 [4],

Equation 24

$$\Delta f = \frac{1}{2T_{\text{int}}}$$

where T_{int} is ROIC integration time [sec], and

Equation 25

$$D^* = \frac{\sqrt{A_D \Delta f}}{NEP}$$

in which A_d is detector area [cm^2], and Δf is the noise bandwidth [Hz]. Results of the detectivity calculations are shown in Figure 32 and Table 11.

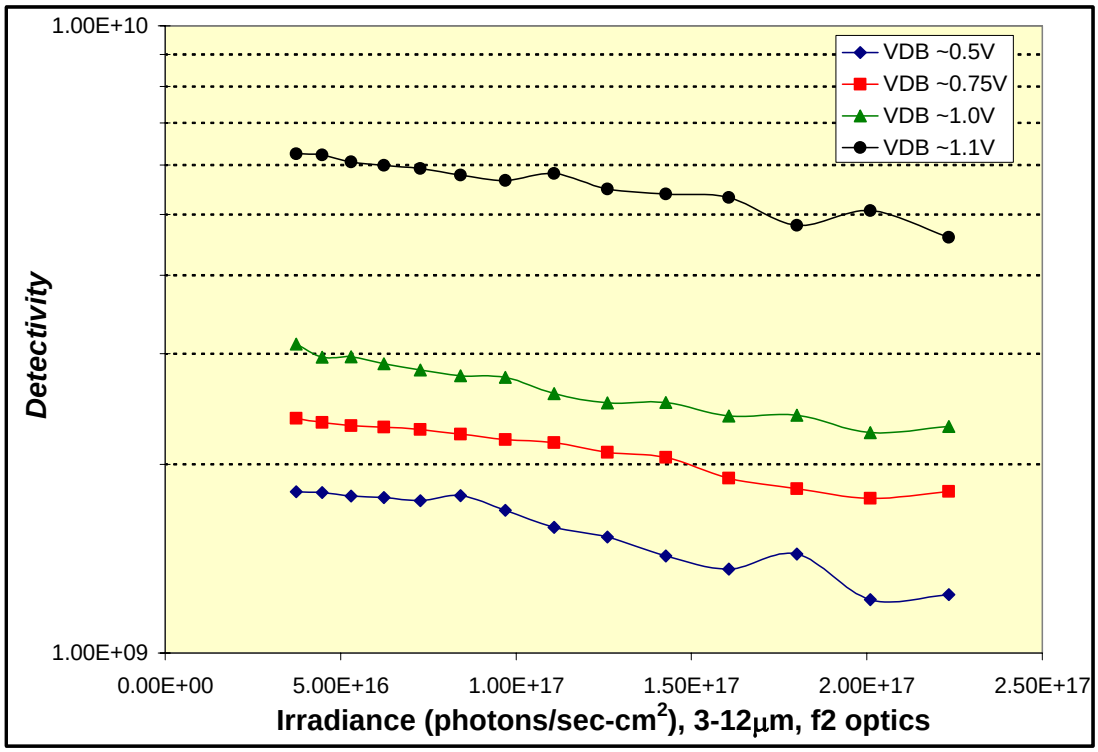

Figure 32. Detectivity versus Irradiance at 77K

Table 12. Peak Detectivity Results at 77K

V_{DB}	D^* $(cm^2Hz)^{1/2}/W$
0.5	1.807E+09
0.75	2.368E+09
1.0	3.109E+09
1.1	6.250E+09

Under the conditions where photon noise dominates (BLIP), the theoretical BLIP detectivity may be used to estimate the QE of a photodetector. Theoretical BLIP detectivity is calculated by Equation 26 [4],

Equation 26

$$D^*_{BLIP} = \frac{\lambda}{2hc}\sqrt{\frac{\eta}{E_q}}$$

where λ is the wavelength [μm], h is Planck's constant [6.626 x 10^{-34}J-s], c is the speed of light [2.998 x 10^8 m/s], η is detector quantum efficiency [electrons per photon] and E_q is photon irradiance [photons/sec-cm^2]. The BLIP detectivity estimate was made using Equation 26 plotted against irradiance at two different values of QE. This plot is compared to the DWELL FPA detectivity values for V_{DB} ~0.5V in Figure 33. Using this estimation technique, the quantum efficiency of the DWELL FPA is approximately 0.25 to 0.45% at 77K.

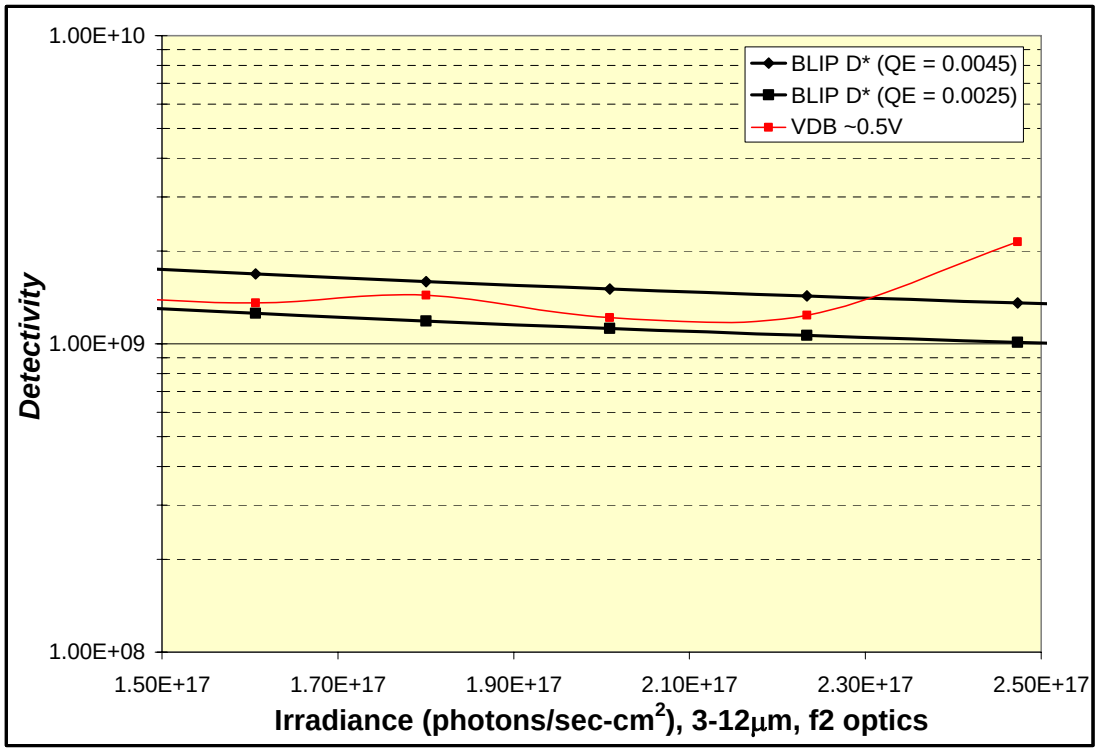

Figure 33. BLIP Detectivity for QE Estimation at 77K

4.5 Noise Equivalent Difference in Temperature (NEDT)

Noise equivalent difference in temperature (NEDT, units of Kelvin) is a performance measure that indicates the smallest difference in uniform scene temperature that a system can detect. A small value of NEDT is preferred because it indicates that a detector can "see" a small difference in scene temperature. The voltage output and noise versus irradiance data collected were used in Equation 27 [4] to calculate the DWELL FPA NEDT,

Equation 27

$$NEDT = \frac{\Delta T}{V_s / V_n}$$

where ΔT is the difference in black body temperatures [K], V_s is the response between two temperatures [V] and V_n is recorded noise voltage at the lower temperature [V]. Minimum NEDT values were observed just prior to the integration capacitor becoming full, where noise decreased due to a decline in readout noise. NEDT is plotted versus detector output in Figure 34 and minimum NEDT values are reported in Table 13.

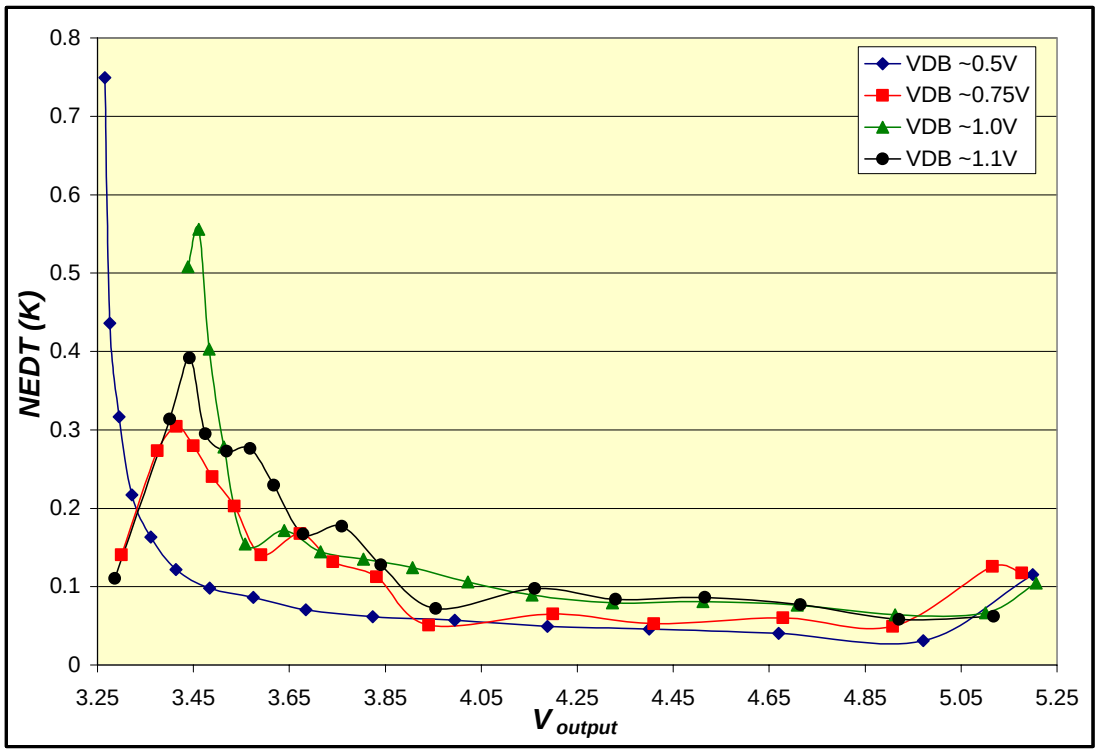

Figure 34. NEDT versus FPA Output Voltage at 77K

Table 13. Minimum NEDT Results at 77K

V_{DB}	NEDT (K)
0.5	0.031
0.75	0.049
1.0	0.064
1.1	0.058

4.6 Brief Comparison to State of the Art Devices

To put the calculated figures of merit for the DWELL FPA into perspective, it is useful to consider recorded performance measures from some commercial and other research IR detector devices. Table 14 below lists some reported D* and NEDT values (from [2]). These numbers are useful to consider when examining the figures of merit reported here for the broadband, MWIR, and LWIR experiments.

Table 14. NEDT and D* Values of Different State of the Art IR Detectors [2].

Detector	Material	Temp (K)	Spectral Range	NEDT (mK)	D* $(cm^2Hz)^{1/2}/W$
DRS Technologies Missile Seeker IRFPA Module	HgCdTe	77	MWIR	---	$4x10^{10}$
			LWIR	---	$3.5x10^{9}$
Indigo Systems, Inc Phoenix Camera	InSb	77	MWIR	25	---
	GaAs QWIP	Stirling Cycle	LWIR	35	---
Army Research Laboratory	70 layer InAs/GaAs QDIP	175	MWIR	---	$4.15x10^{7}$
NASA Jet Propulsion Laboratory	70 layer InAs/GaAs QDIP	150	MWIR	50	$3.7x10^{10}$

It is promising to note that the NEDT and D* values calculated for the DWELL FPA operating at 77K are comparable to those shown in Table 14 at the same operating temperature. MWIR and LWIR values for NEDT and D* are reported in Chapter 5.

Chapter 5

5 Two-Color Performance

Along with the previously reported information of unfiltered performance, the two-color performance of the DWELL FPA was measured by separately recording MWIR and LWIR response data. The performance in each band was evaluated by filtering the incident flux of photons with commercially available band pass IR lenses that allowed 3-5μm in the MWIR and 8-12μm in the LWIR region to illuminate the FPA. All of the performance measurements reported here were made at a nominal FPA temperature of 77K. Integration times used in testing are as shown in Table 5.

5.1 Mid-Wave and Long-Wave IR Noise Measurements

FPA temporal noise was measured versus photon irradiance for both the MWIR and LWIR responses at the four detector biases of ~0.5, 0.75, 1.0, and 1.1V. Noise data demonstrated a roll off at high irradiances, with data for VDB ~1.0 and ~ 1.1V modestly showing this effect because the experiments were not continued through to the point of the integration capacitors being full. Plots of the MWIR and LWIR noise versus irradiance are shown in Figure 35 and Figure 36.

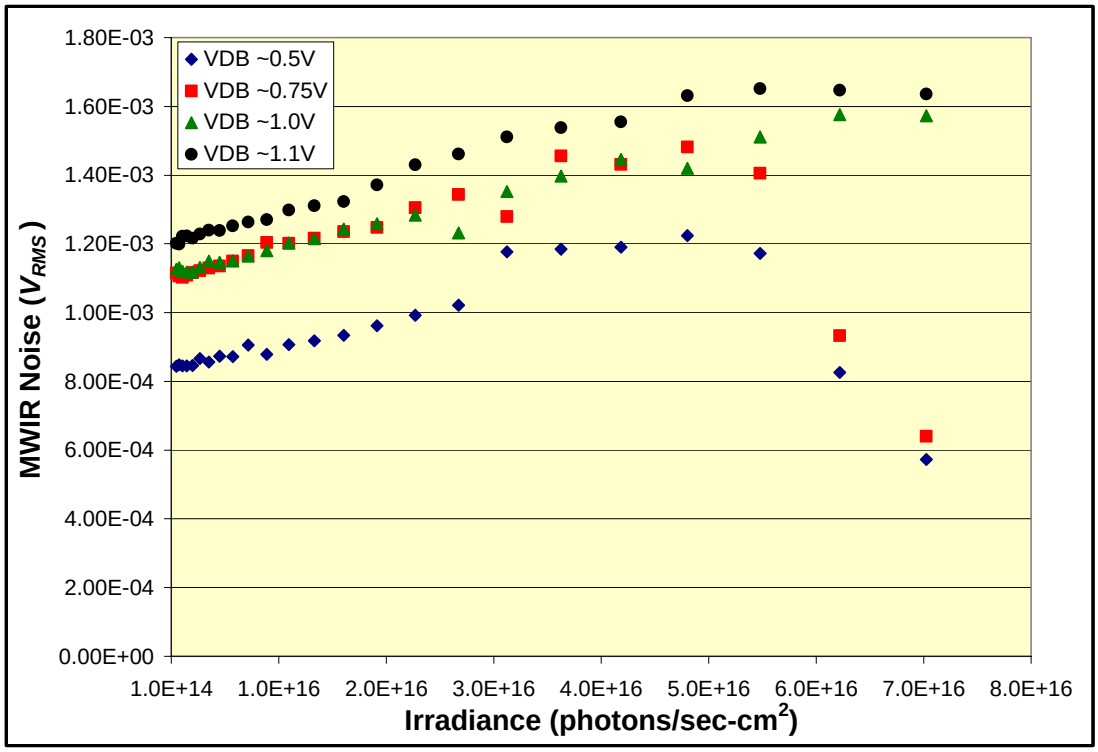

Figure 35. DWELL FPA MWIR Noise versus Irradiance at 77K

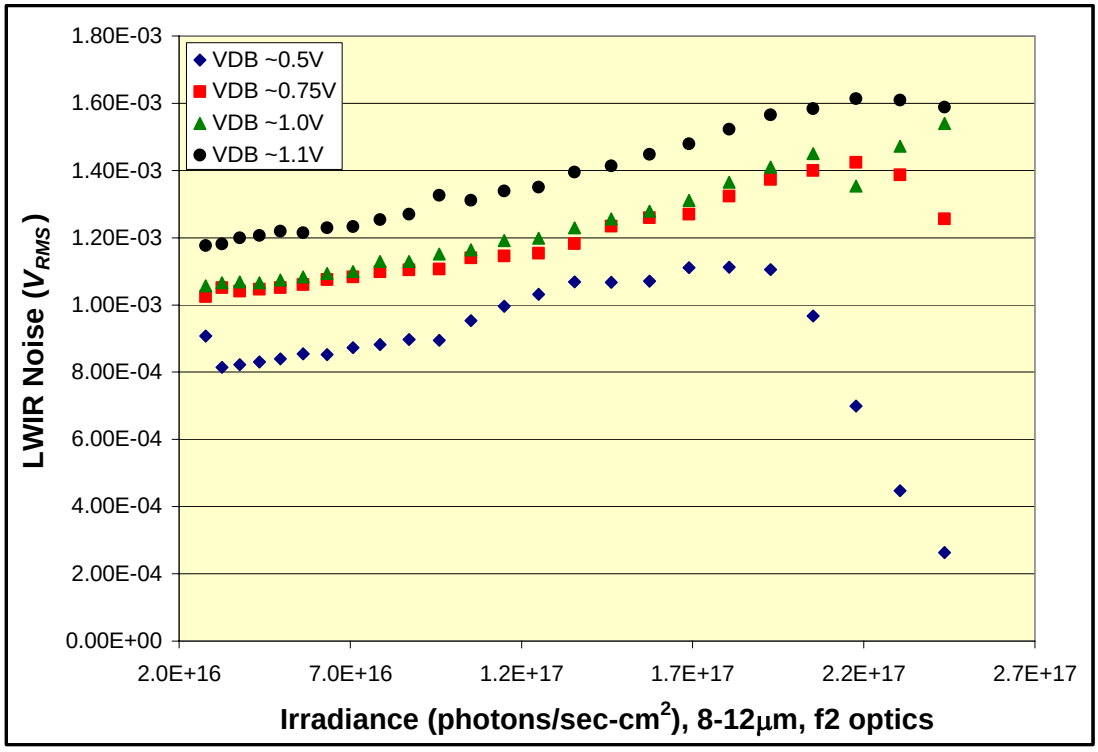

Figure 36. DWELL FPA LWIR Noise versus Irradiance at 77K

5.2 Responsivity

Peak responsivity in the MWIR and LWIR bands was determined from the recorded FPA output voltage (V_{output}) versus irradiance data (shown in Figure 37) at the four test biases using Equations 20 and 21, each evaluated at 3-5µm and 8-12µm for MWIR and LWIR bands, respectively. FPA output voltage is plotted for the MWIR and LWIR bands separately in Figure 38 and Figure 39, respectively. MWIR and LWIR voltage responsivities (V/W) are plotted for each bias versus irradiance in Figure 40 and Figure 41. Peak responsivities from each band are shown in Table 15.

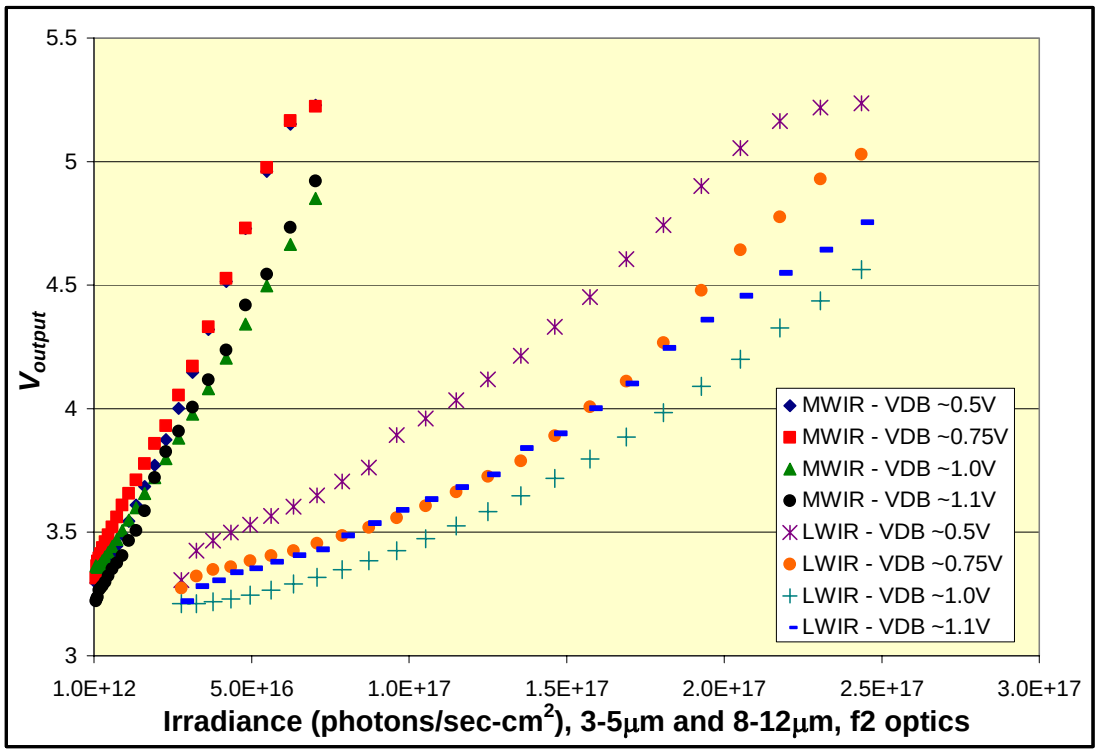

Figure 37. MWIR and LWIR Output Voltage versus Irradiance at 77K

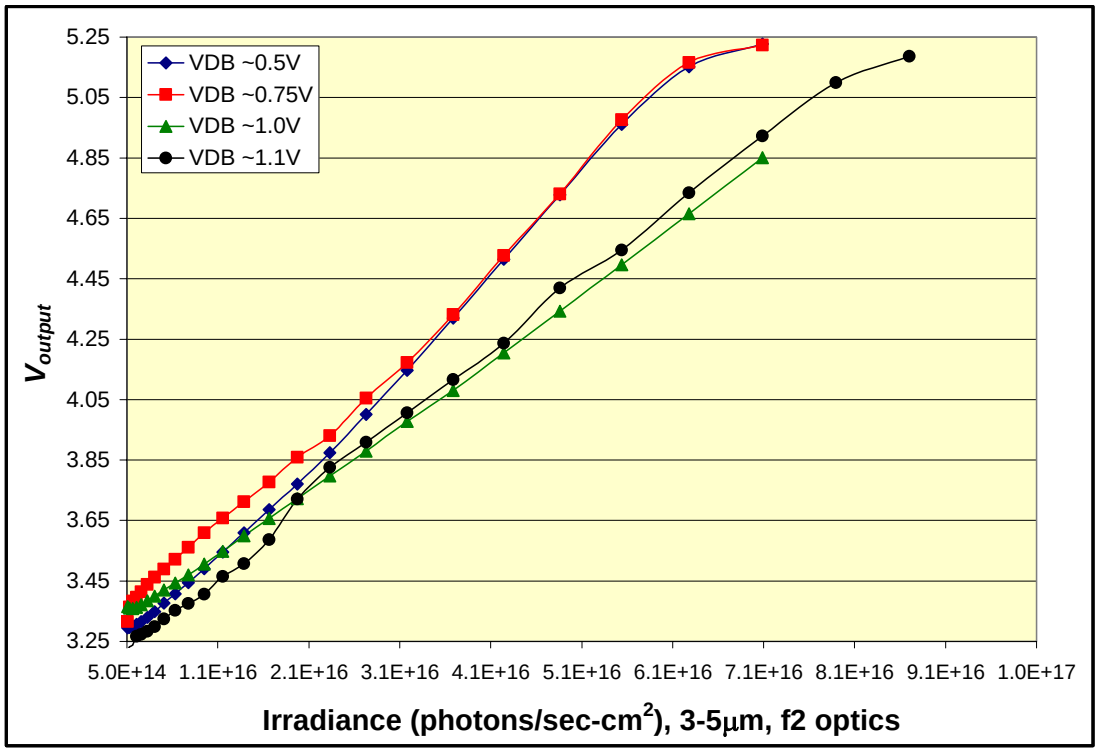

Figure 38. MWIR Output Voltage versus Irradiance at 77K

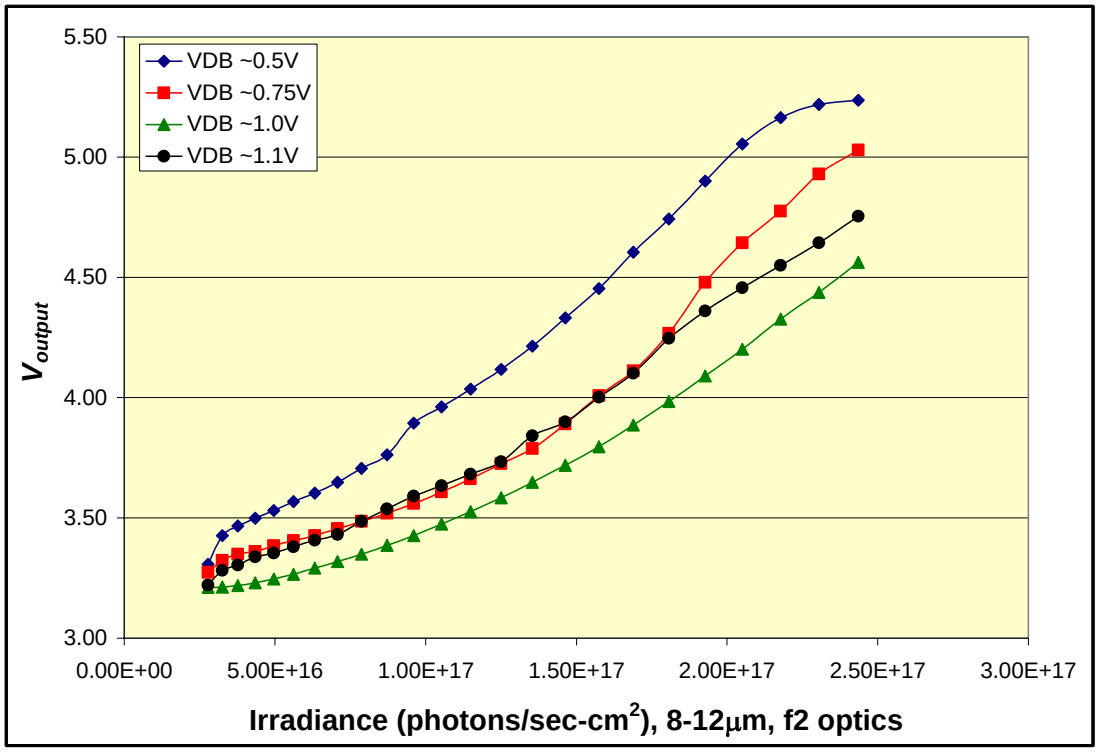

Figure 39. LWIR Output Voltage versus Irradiance at 77K

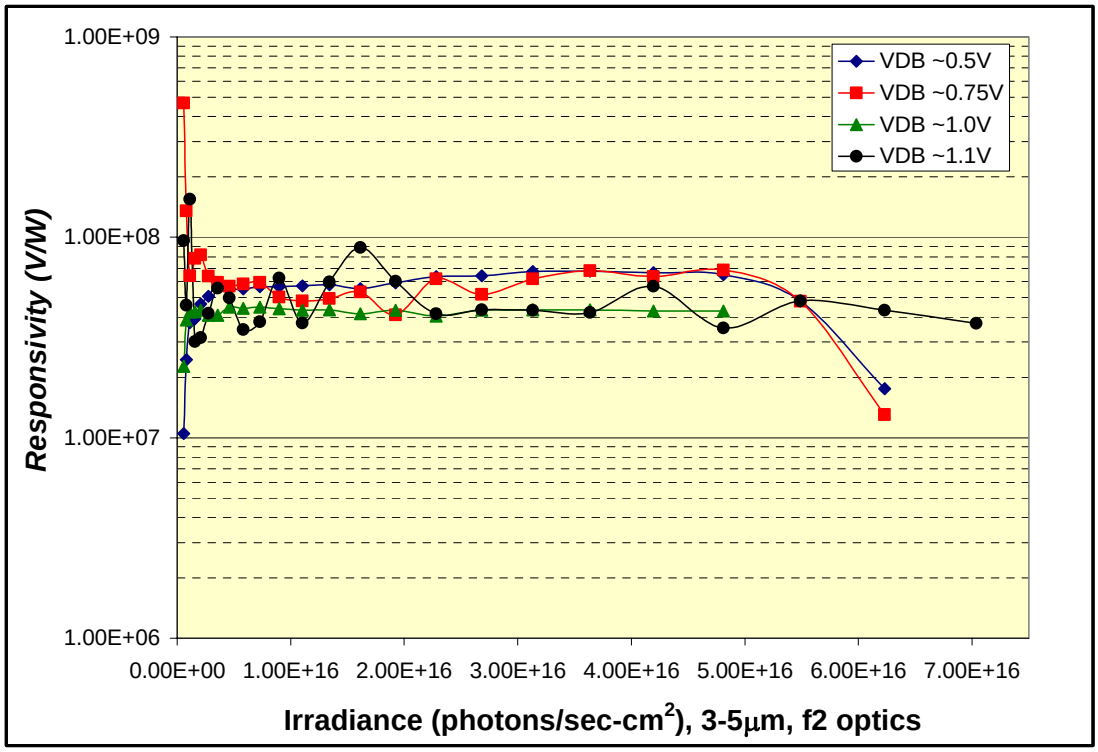

Figure 40. MWIR Responsivity versus Irradiance at 77K

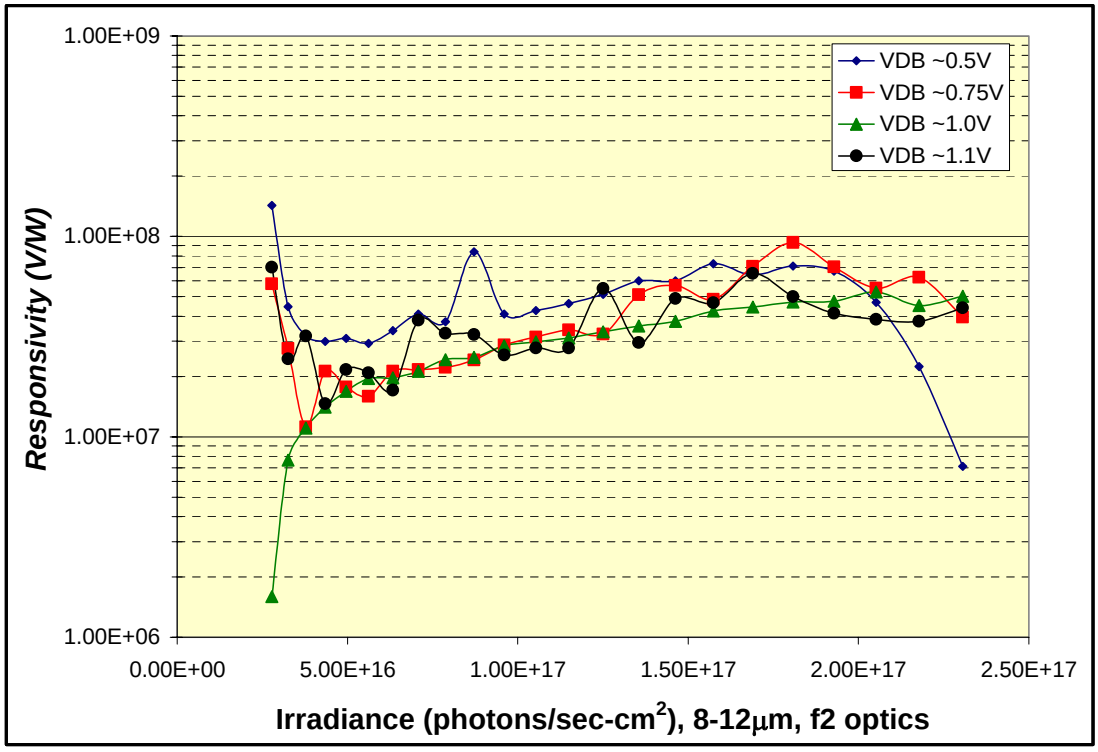

Figure 41. LWIR Responsivity versus Irradiance at 77K

Table 15. MWIR and LWIR Responsivity Results at 77K

V_{DB}	R_v (V/photon)	R_v (V/W)
MWIR		
0.5	1.392E-09	6.763E+07
0.75	2.081E-08	4.677E+08
1.0	9.438E-09	4.491E+07
1.1	4.171E-08	1.547E+08
LWIR		
0.5	6.299E-10	7.299E+07
0.75	1.875E-09	9.345E+07
1.0	4.765E-09	5.282E+07
1.1	8.475E-09	7.035E+07

As the ROIC integration capacitors reach full well capacity, both the MWIR and LWIR responsivities began to fall off at high irradiances.

Based on previous spectral response experiment results from similar devices, it was to be expected that the DWELL FPA would exhibit better responsivity in the MWIR band. The results tabulated here reflect that the MWIR responsivity is generally higher than the LWIR data reflects as V_{DB} was increased, though they are on the same order of magnitude. This reflects the spectral response data collected with the DWELL FPA (Figure 25 and Figure 26 – discussed in section 3.4.2).

5.3 Noise Equivalent Power (NEP)

Focal plane array NEP values were calculated in the MWIR and LWIR using the two-color responsivity data and measured detector noise values (refer to Equation 22). Results of these calculations are displayed in Figures 46-49 in Appendix A. Minimum

NEP values are presented in Table 16.

Table 16. MWIR and LWIR Minimum NEP Values at 77K

V_{DB}	NEP (W)
MWIR	
0.5	1.465E-11
0.75	2.365E-12
1.0	2.628E-11
1.1	7.901E-12
LWIR	
0.5	1.068E-11
0.75	1.469E-11
1.0	2.562E-11
1.1	1.683E-11

5.4 Noise Equivalent Irradiance (NEI)

DWELL FPA MWIR and LWIR values of NEI were calculated from Equation 23 and are displayed in Figures 50-53 in Appendix B. Minimum NEI values are displayed in Table 17.

Table 17. MWIR and LWIR Minimum NEI Values at 77K

V_{DB}	NEI (photons/cm^2)
MWIR	
0.5	1.296E+11
0.75	9.226E+09
1.0	2.184E+10
1.1	5.087E+09
LWIR	
0.5	1.171E+11
0.75	1.271E+11
1.0	4.931E+10
1.1	2.491E+10

In general, the NEP and NEI values tend to remain fairly flat with a slight decrease at higher irradiances in the MWIR band and show a decrease in the LWIR band as irradiance increased toward the ROIC full well condition.

5.5 Detectivity (D*)

DWELL FPA detectivity was calculated in the MWIR and LWIR bands and is plotted in Figures 54-57 in Appendix C. Maximum recorded detectivity values are tabulated in Table 18; average detectivity values at each bias are listed in Table 19.

Table 18. Maximum MWIR and LWIR Detectivity at 77K

V_{DB}	$D^*\ (cm^2Hz)^{1/2}/W$
MWIR	
0.5	2.382E+09
0.75	2.254E+10
1.0	4.302E+09
1.1	1.652E+10
LWIR	
0.5	6.120E+09
0.75	3.628E+09
1.0	4.413E+09
1.1	7.758E+09

Table 19. Average Measured Detectivity

V_{DB}	Average D* $(cm^2Hz)^{1/2}/W$
MWIR	
0.5	1.876E+09
0.75	3.572E+09
1.0	3.722E+09
1.1	5.179E+09
LWIR	
0.5	1.954E+09
0.75	1.733E+09
1.0	2.651E+09
1.1	3.617E+09

Detectivity for MWIR and LWIR response increased with increasing irradiance, with MWIR detectivity being greater than LWIR detectivity . Maximum D* values tended to occur near full well where detector noise is reduced.

5.6 Noise Equivalent Difference in Temperature (NEDT)

To calculate NEDT in the MWIR and LWIR bands, noise voltage versus irradiance data was evaluated with Equation 27. The resulting data was plotted versus detector output voltage in Figures 58-61 in Appendix D. The minimum observed NEDT values are shown in Table 20.

Table 20. Minimum MWIR and LWIR NEDT at 77K

V_{DB}	NEDT (K)
MWIR	
0.5	0.043
0.75	0.049
1.0	0.085
1.1	0.073
LWIR	
0.5	0.063
0.75	0.065
1.0	0.107
1.1	0.066

NEDT values were observed to be quite high at low photon fluxes because of the low signal-to-noise ratio under these conditions. Minimum NEDT values were noted near the full well voltages of the ROIC capacitors as the reset noise contribution to detector noise began to drop.

5.7 Review of Two-Color Performance

By reviewing the two-color response performance measures, one can see that the figures of merit calculated tend to be better in the MWIR region, though the difference between MWIR performance and LWIR performance was not dramatically different at the four detector biases used in testing. This is attributed to the fact that the MWIR and LWIR responses are comparable at these lower detector biases (see Figure 25 and Figure 26), where bound-to-continuum energy transitions are favored leading to a slightly larger MWIR response. At larger reverse bias the LWIR response would be expected to become dominant (as reflected in Figure 27) because the probability of carriers tunneling

from the bound-to-bound and bound-to-quasi-bound states increases, leading to the increased LWIR response. With the 9705 ROIC two-color response is noted from the measured spectral response of the FPA, but because of the limitation of biases that can be applied with the 9705, the concept of a bias tunable FPA camera could not be more thoroughly explored.

Chapter 6

6 Future Work and Conclusions

6.1 Exploring FPA Spectral Diversity

The pixels of the DWELL FPA are each slightly different than their neighboring pixels due to issues with array processing, hybridization, and applied detector bias. These small differences may reveal themselves as small differences in individual pixel response at a given bias. These small differences could potentially be utilized to extract additional spectral information from collected scene images. Considering how the human eye focuses light onto the retina, which is composed of three different classes of spectral receptors with highly overlapping spectral response, the idea of an "infrared retina" was proposed. In the IR retinal system, neighboring pixels have different applied bias voltages, and hence different spectral responses. Figure 58 illustrates the motivation behind exploring the IR retina idea. Response curves of the L, M and S cones are plotted on the left. On the right, spectral response curves are shown for a DWELL detector at six different biases. Notice the change in spectral response that appears to mimic the spectral response of the cones in the human eye. With this idea in mind, several pixels were selected to begin searching for differences in spectral response of individual pixels. The responses of several pixels are plotted in Figure 59.

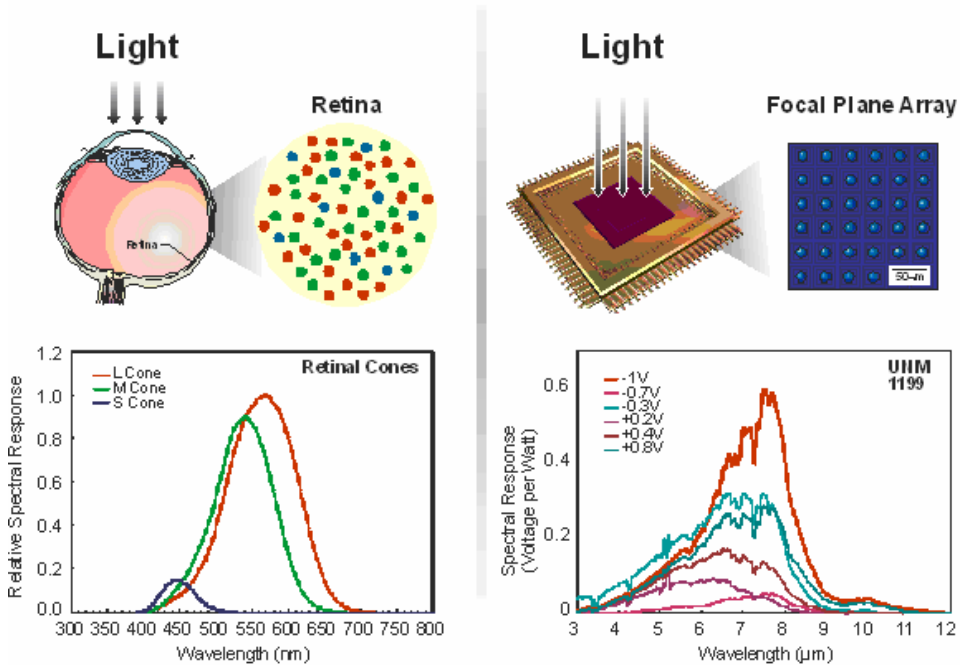

Figure 42. Exploring the IR Retina: Response of the Cones in a Human Eye May be Mimicked by Spectral Diversity within the Pixels of the DWELL FPA

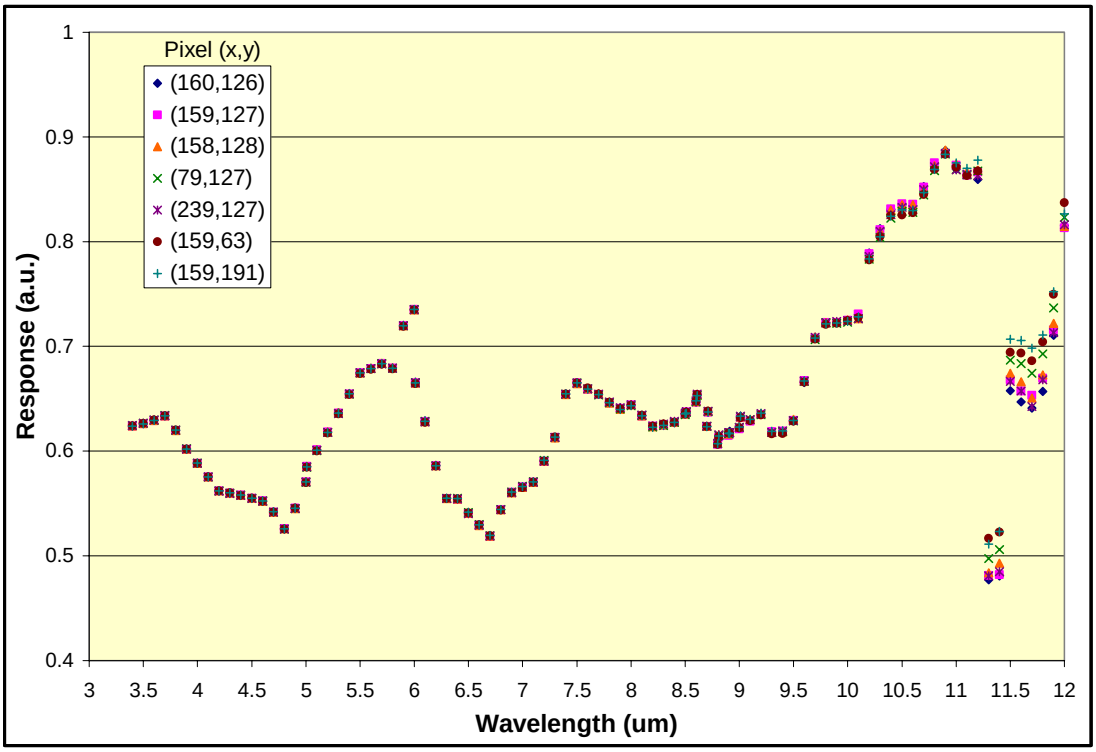

Figure 43. Response from Selected FPA Pixels at a Detector Bias of -0.5V.

The data presented in Figure 59 shows nearly identical responses from each pixel. This initial investigation of pixel spectral diversity did not yield information regarding the likelihood of an IR retina using the DWELL FPA. With a different ROIC it is possible that at larger biases some differences may emerge allowing for more exploration of the infrared retina idea. Another approach may be to devise a ROIC that applies different voltage biases at individual pixels within the array in an attempt to create "IR cones", or pixel sets that have slightly different and overlapping spectral response curves similar to the cones in the human retina. Future measurements will be necessary as well as the development of algorithms for processing the pixel data to optimize spectral sensing. These efforts will leverage the ongoing work of other research group members

investigating methods of implementing spectral filters without the need for additional optics.

6.2 Comparison of the DWELL FPA to HgCdTe Two-Color Detectors

Infrared detectors based on the HgCdTe (mercury-cadmium-telluride, or MCT) material system remain an industry standard today. The adjustable band gap and the maturity of the material platform has led to the emergence of high-performance two-color HgCdTe detectors [19]. It is noteworthy to compare the DWELL FPA to the current state-of-the-art HgCdTe detectors to provide guidance on how to improve the DWELL FPA to meet new application requirements. Two-color HgCdTe detectors are constructed of n-p^+-n triple layer structures, forming two back-to-back p-n junctions like the structure shown in Figure 60. Two-color responses cannot be obtained simultaneously from HgCdTe structures because only one of the p-n junctions can be biased at a given time to collect photons. To collect information from both bands the bias polarity must be alternated. With the DWELL detector, MWIR and LWIR photons can be collected simultaneously at a given detector bias (although currently the MWIR and LWIR responses cannot be distinguished without changing the bias). The QE of HgCdTe devices are substantially higher (approximately 70% [19]) than that of DWELL devices, allowing for stronger responsivity. Despite this shortcoming in QE, detectors based on III-IV materials, like the DWELL, are appealing because of manufacturing difficulties, FPA fragility [8] and material problems [19] of the HgCdTe material platform. The efforts taken with the DWELL FPA follow in the same vein as the two-color HgCdTe work and offers some

potential advantages of a bias tunable FPA and simultaneous MWIR and LWIR responses.

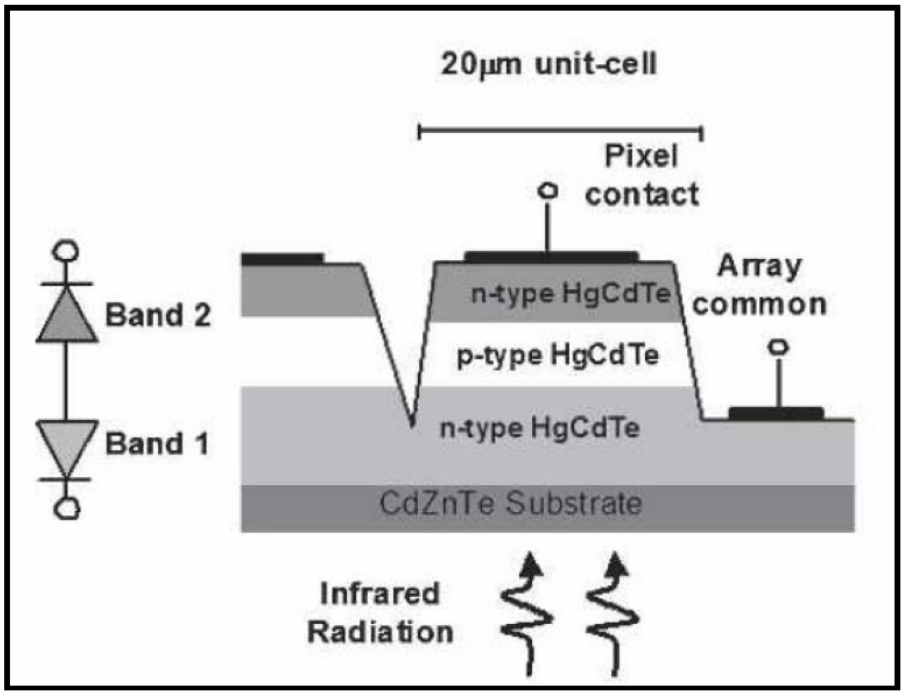

Figure 44. HgCdTe Two-Color Single Pixel Detector [19].

6.3 Conclusions

Based on the collected information and calculated values, the DWELL FPA appeared to perform slightly better in the MWIR band than in the LWIR band. Mid-wave response for the DWELL should be dominant at the detector biases between ~0.5-1.1V because the electrons from MWIR response have a higher likelihood of being collected over the electrons due to LWIR response. LWIR response is expected to improve and become dominant as the detector bias is increased. This is because carriers promoted from bound-to-bound transistions have a higher tunneling probability since the increased

applied electric field across the active region results in a greater tilting of the energy bands (see Figure 61). Higher detector biases generally result in increased noise levels, potentially degrading FPA figures of merit. This was observed and resulted in the general degradation of NEP, NEI, D* and NEDT. In the investigation of FPA spectral tunability care must be taken to determine the optimum operating voltages.

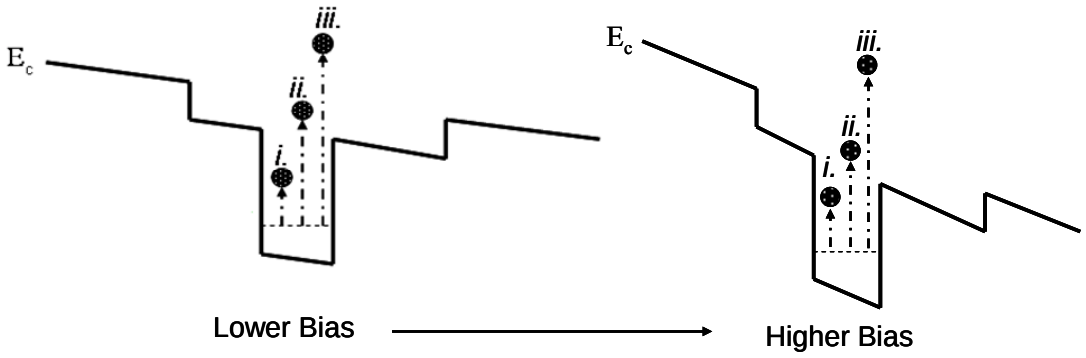

Figure 45. DWELL Energy Bands at Different Biases.

Future developments with the DWELL FPA will include improving detector performance by increasing quantum efficiency, which will have a positive impact on device figures of merit. One method for improving QE includes investigation of increased active region size (adding DWELL stacks), though this method will be limited by material strain introduced by adding more stacks to the structure. Compressive strain introduced by each QD layer will, at some point, cause defects that will degrade material quality and adversely impact performance measures. Additional methods for improving QE include adding a photonic crystal cavity and/or increasing detector gain by adding an avalanche photodiode (APD). Other future work will include further exploration of device spectral

diversity and other enhancements such as individual pixel filters to create sub-arrays of detectors staring into different spectral regions.

7 Previously Published Work

Results from the body of work presented in this thesis manuscript have previously appeared in a publication of Applied Physics Letters, Volume 91, Number 8 [22] and were presented at the 2007 SPIE Optics + Photonics conference, Conference 6678: Infrared Spaceborne Remote Sensing and Instrumentation XV (*Demonstration of a 320 x 256 quantum dots-in-a-well focal plane array*, Lenz, et al), to be published in Proceedings of SPIE Vol. 6678.

List of Appendices

Appendix A. – Two-Color Noise Equivalent Power (NEP) Plots

Appendix B. – Two-Color Noise Equivalent Irradiance (NEI) Plots

Appendix C. – Two-Color Detectivity Plots

Appendix D. – Two-Color Noise Equivalent Difference in Temperature (NEDT) Plots

Appendix A. Two-Color Noise Equivalent Power (NEP) Plots

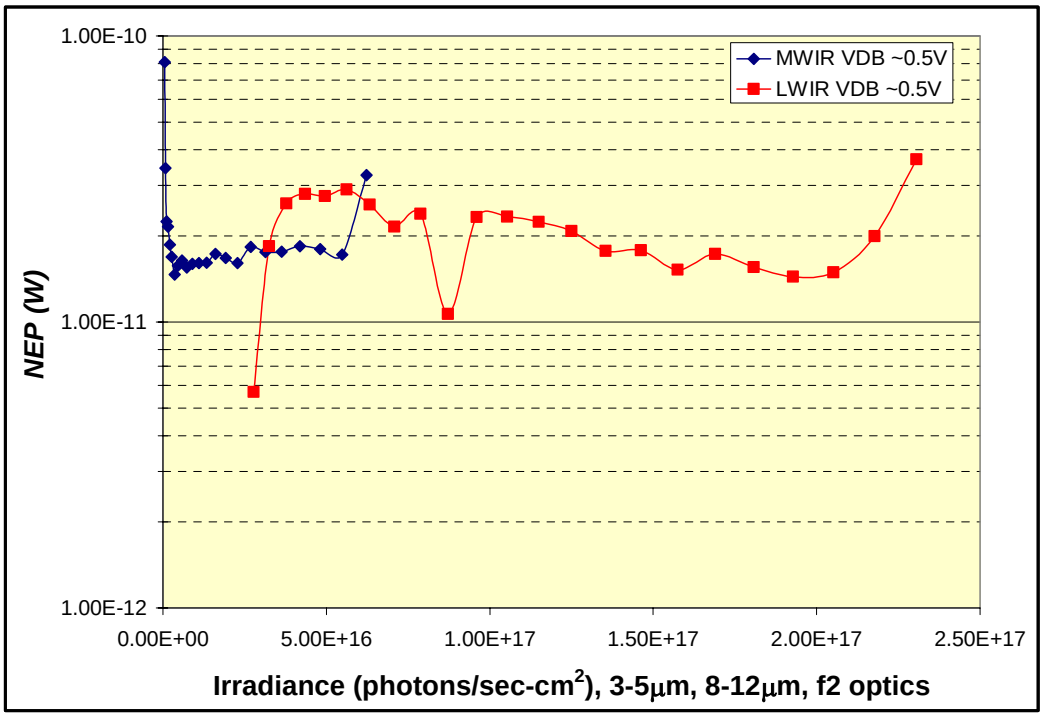

Figure 46. MWIR and LWIR NEP at V_{DB} ~0.5V and 77K

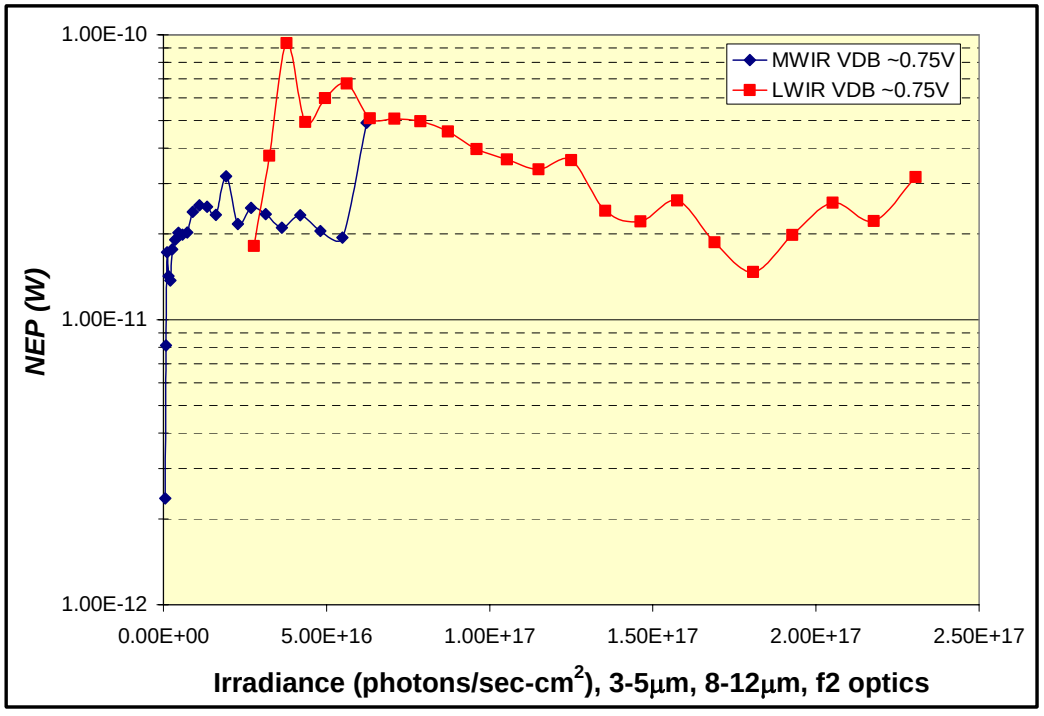

Figure 47. MWIR and LWIR NEP at V_{DB} ~0.75V and 77K

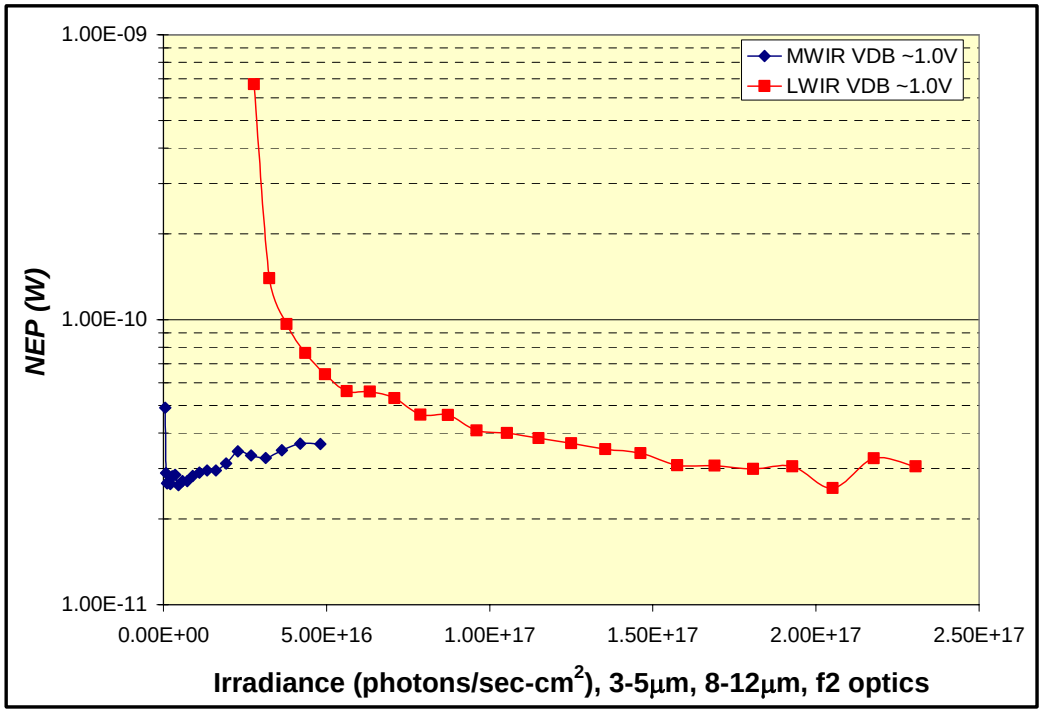

Figure 48. MWIR and LWIR NEP at V_{DB} ~1.0V and 77K

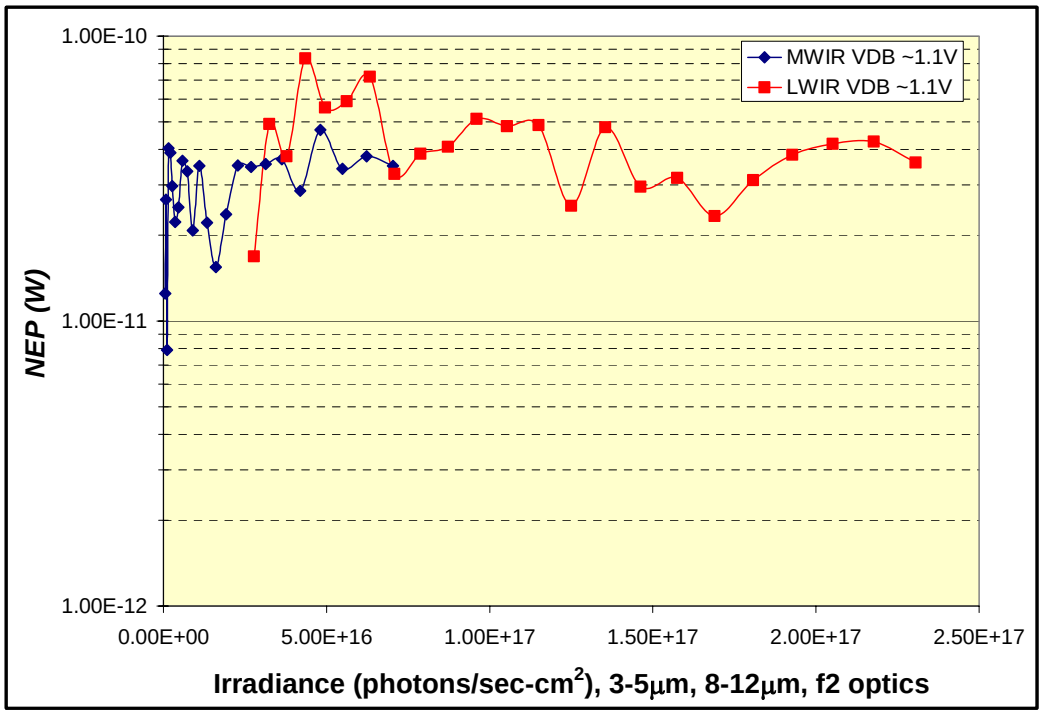

Figure 49. MWIR and LWIR NEP at V_{DB} ~1.1V and 77K

Appendix B. Two-Color Noise Equivalent Irradiance (NEI)

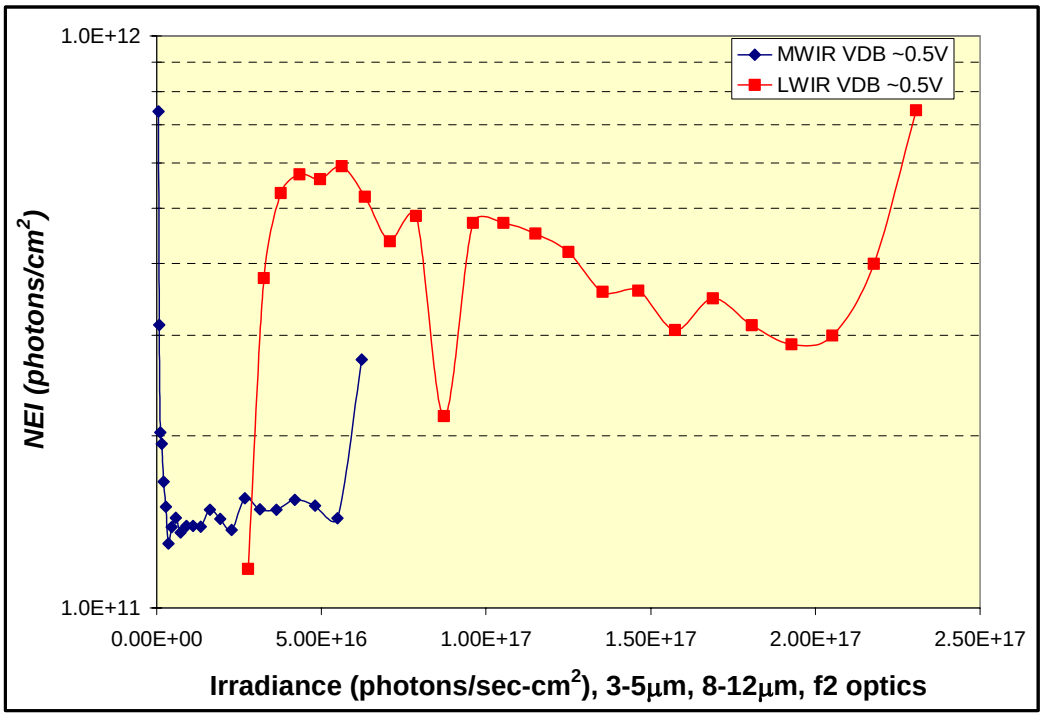

Figure 50. MWIR and LWIR NEI at V_{DB} ~0.5V and 77K

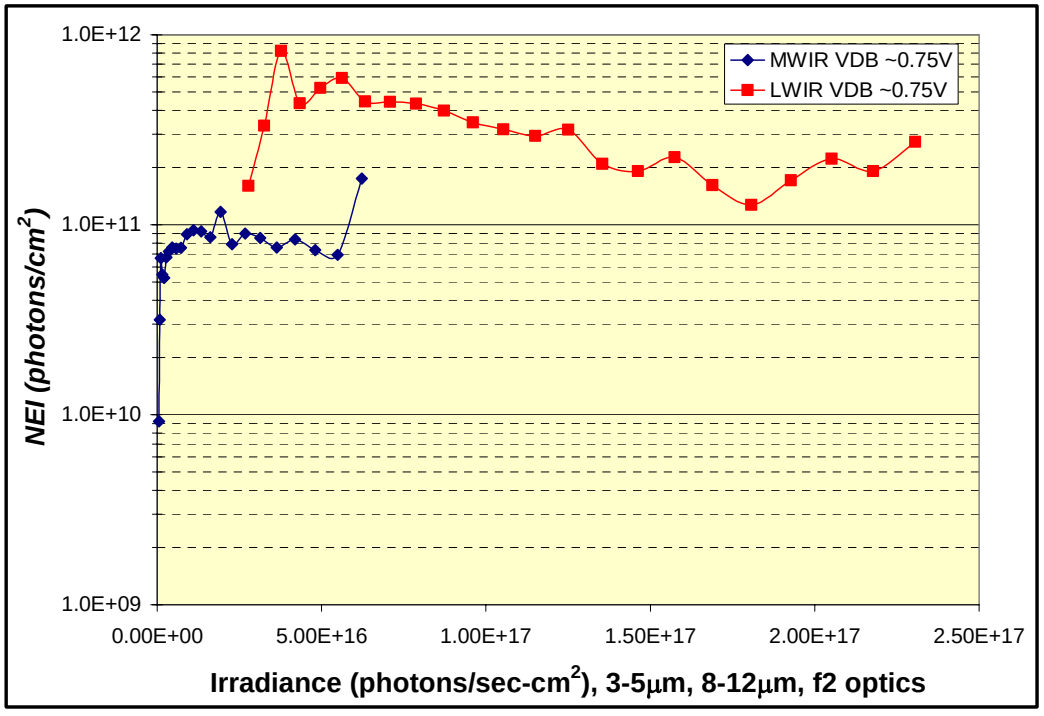

Figure 51. MWIR and LWIR NEI at V_{DB} ~0.75V and 77K

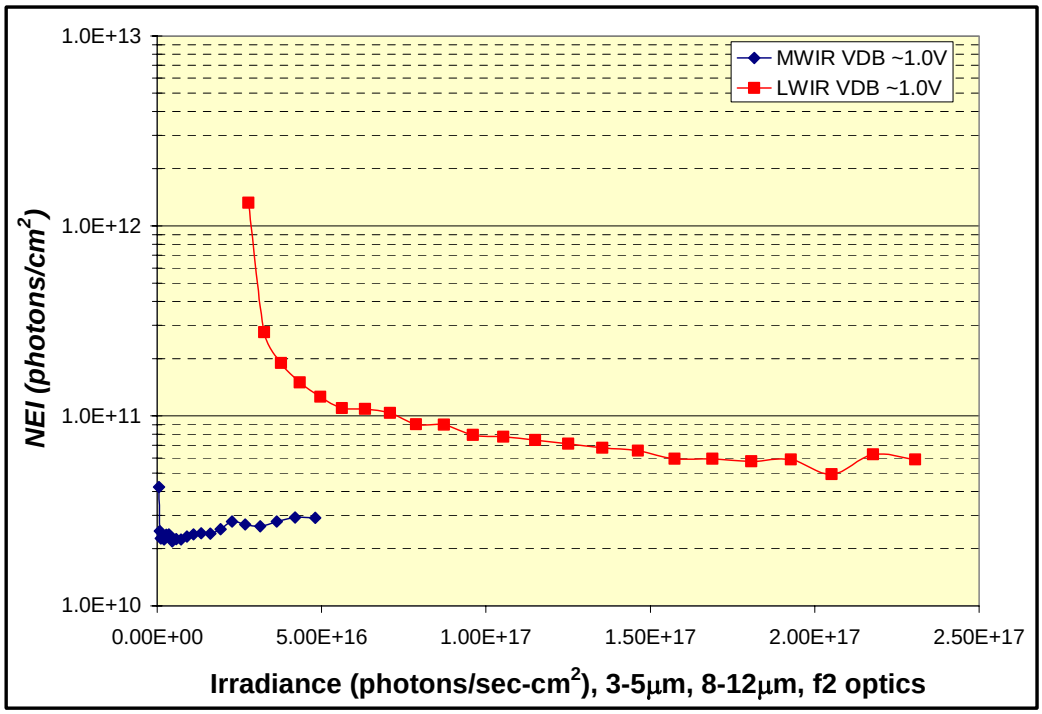

Figure 52. MWIR and LWIR NEI at V_{DB} ~1.0V and 77K

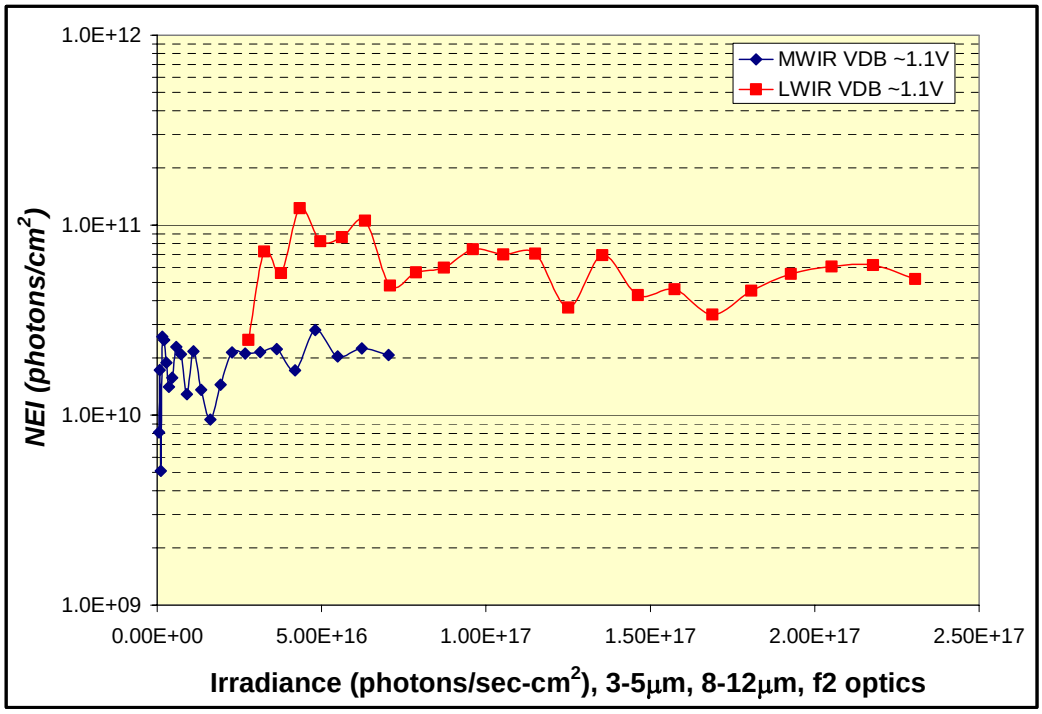

Figure 53. MWIR and LWIR NEI at V_{DB} ~1.1V and 77K

Appendix C. Two-Color Detectivity Plots

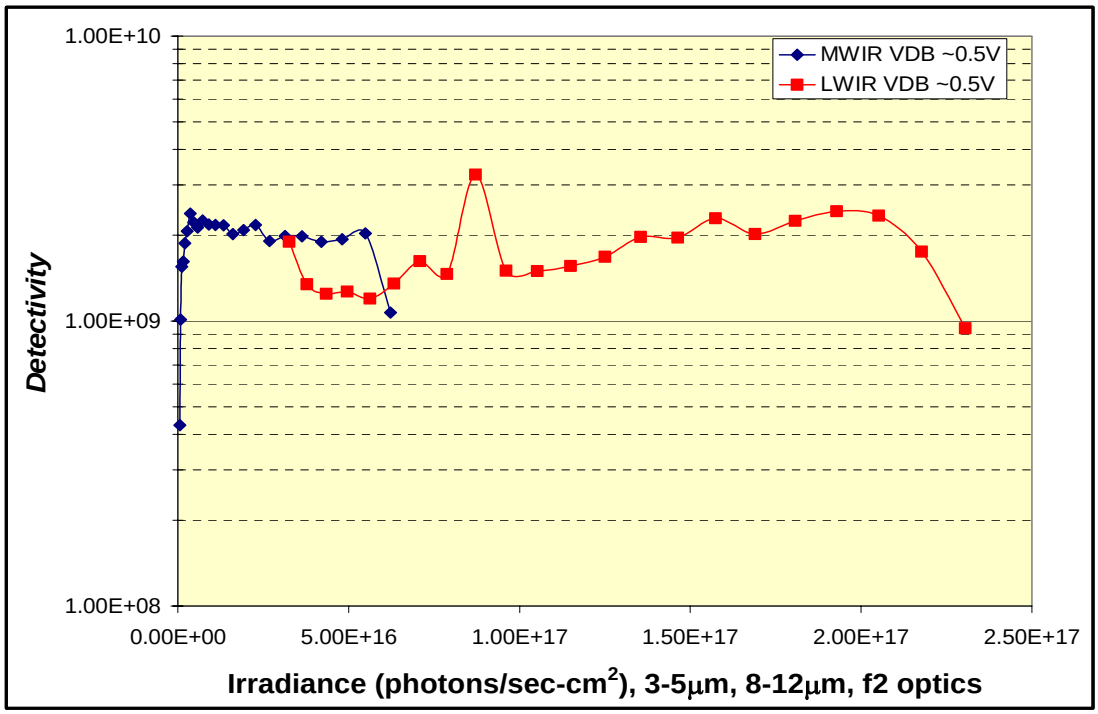

Figure 54. MWIR and LWIR Detectivity at V_{DB} ~0.5V and 77K

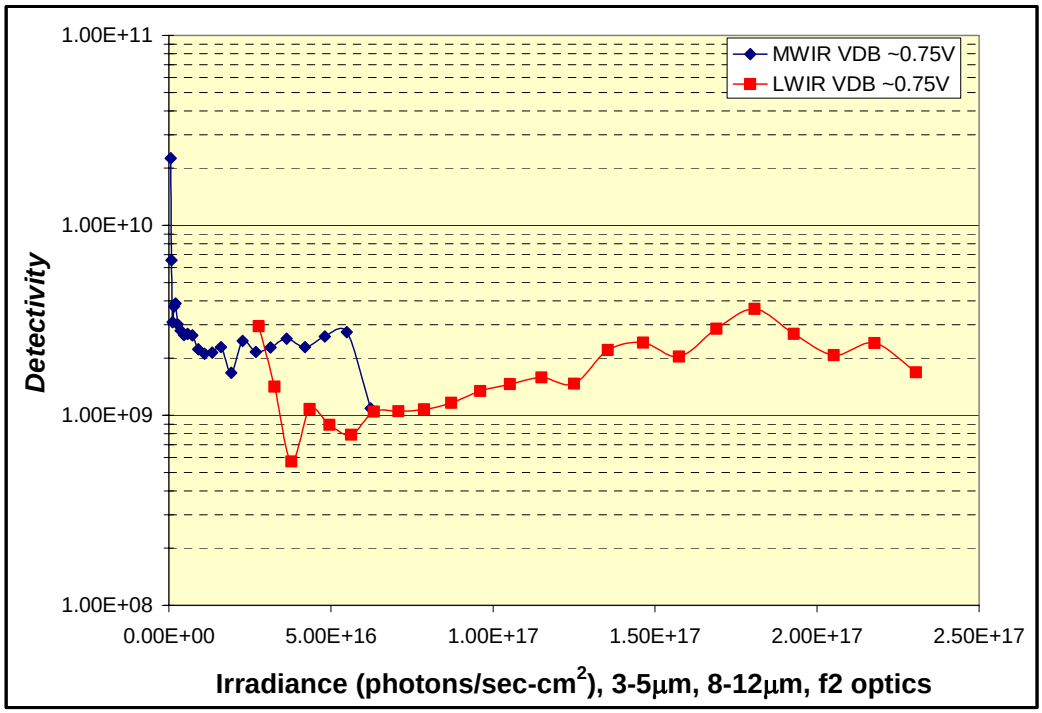

Figure 55. MWIR and LWIR Detectivity at V_{DB} ~0.75V and 77K

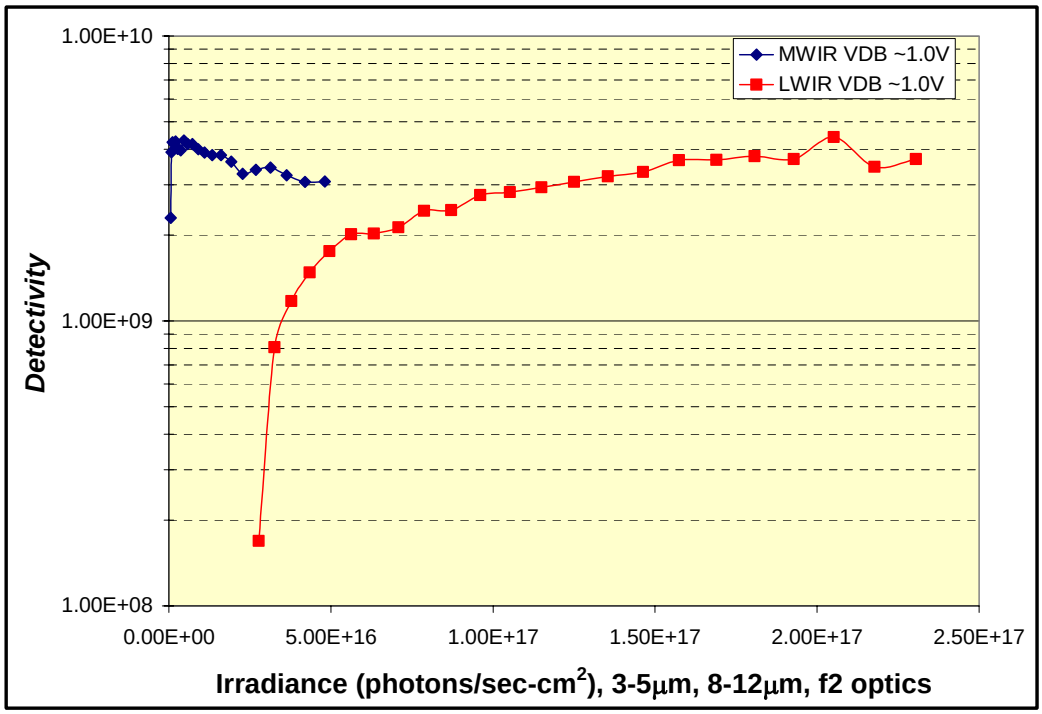

Figure 56. MWIR and LWIR Detectivity at V_{DB} ~1.0V and 77K

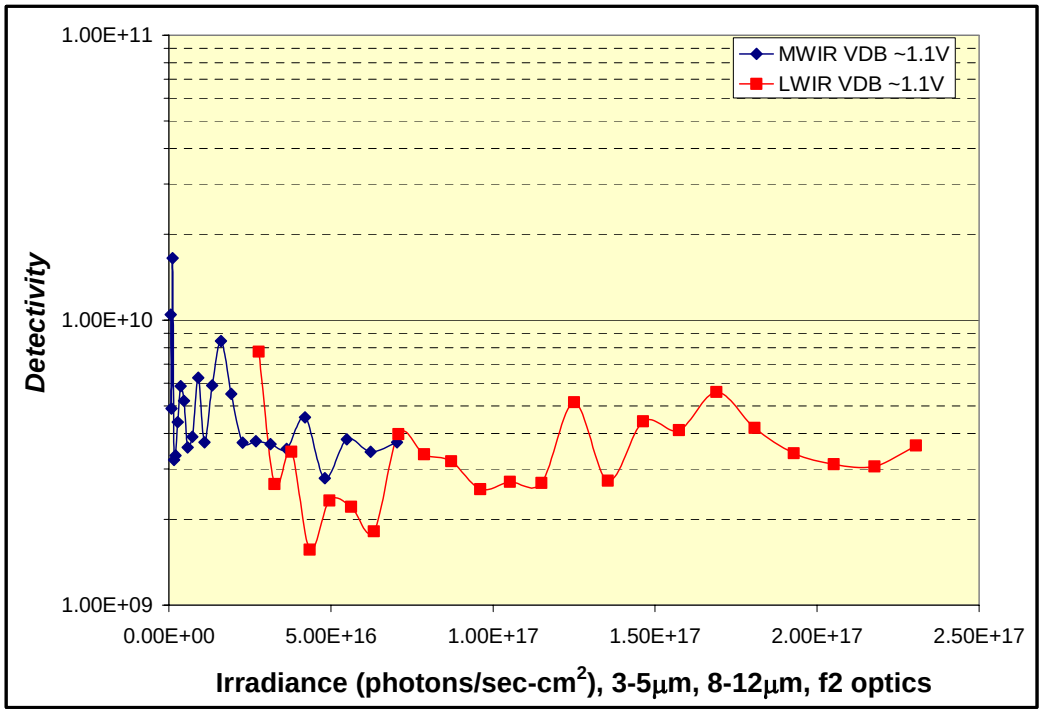

Figure 57. MWIR and LWIR Detectivity at V_{DB} ~1.1V and 77K

Appendix D. Two-Color Noise Equivalent Difference in Temperature (NEDT) Plots

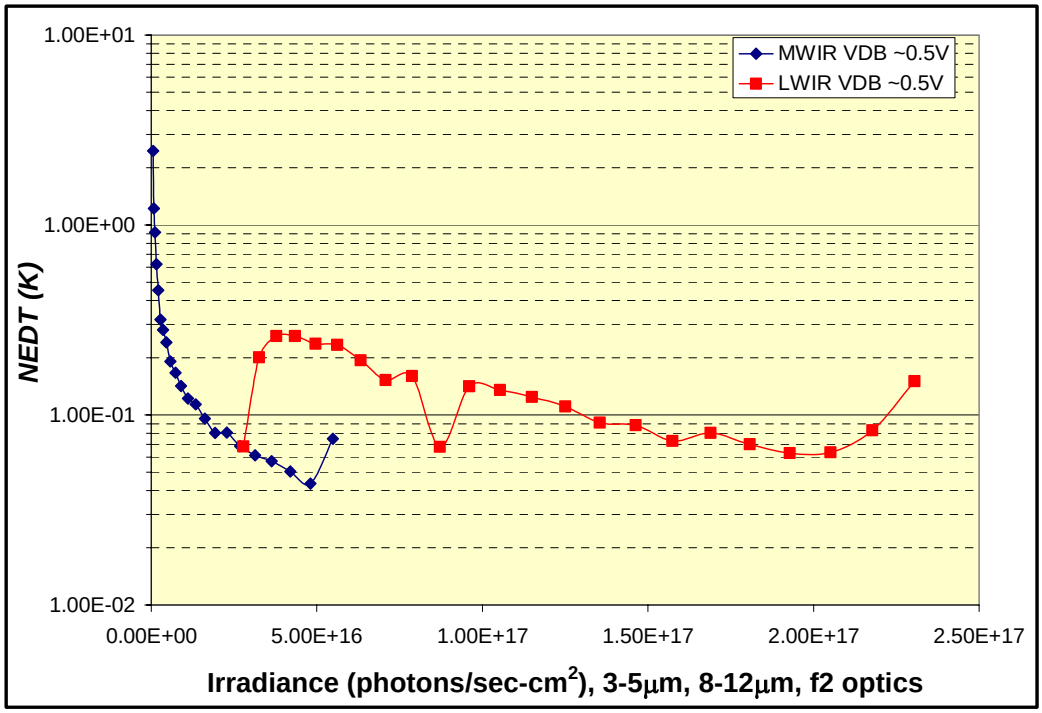

Figure 58. MWIR and LWIR NEDT at V_{DB} ~0.5V and 77K

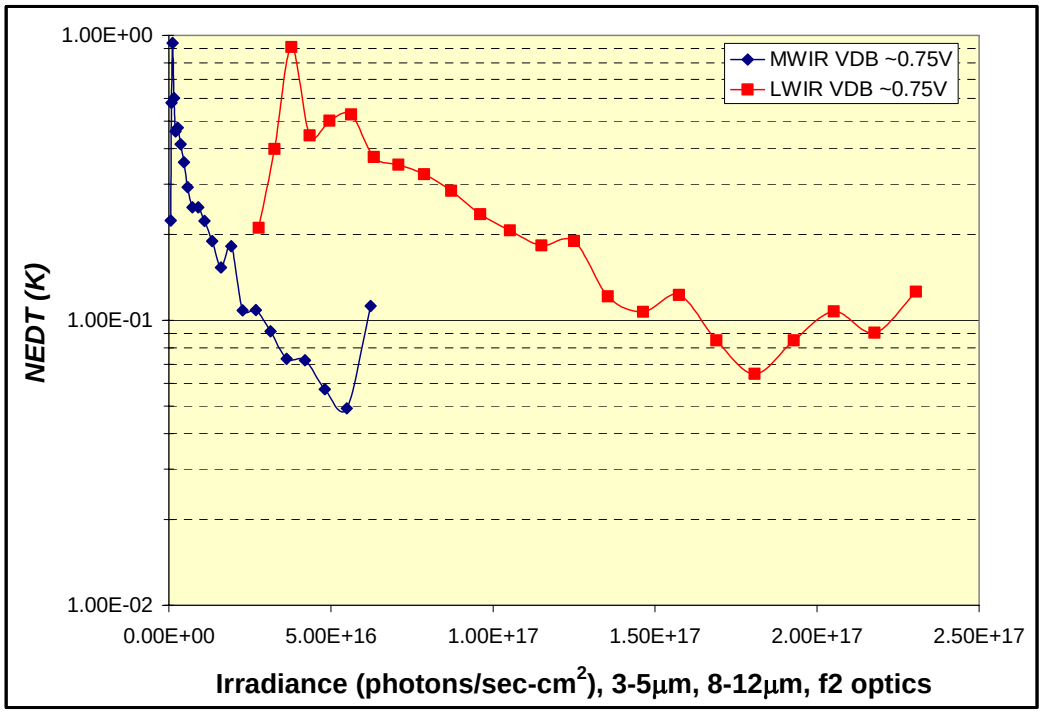

Figure 59. MWIR and LWIR NEDT at V_{DB} ~0.75V and 77K

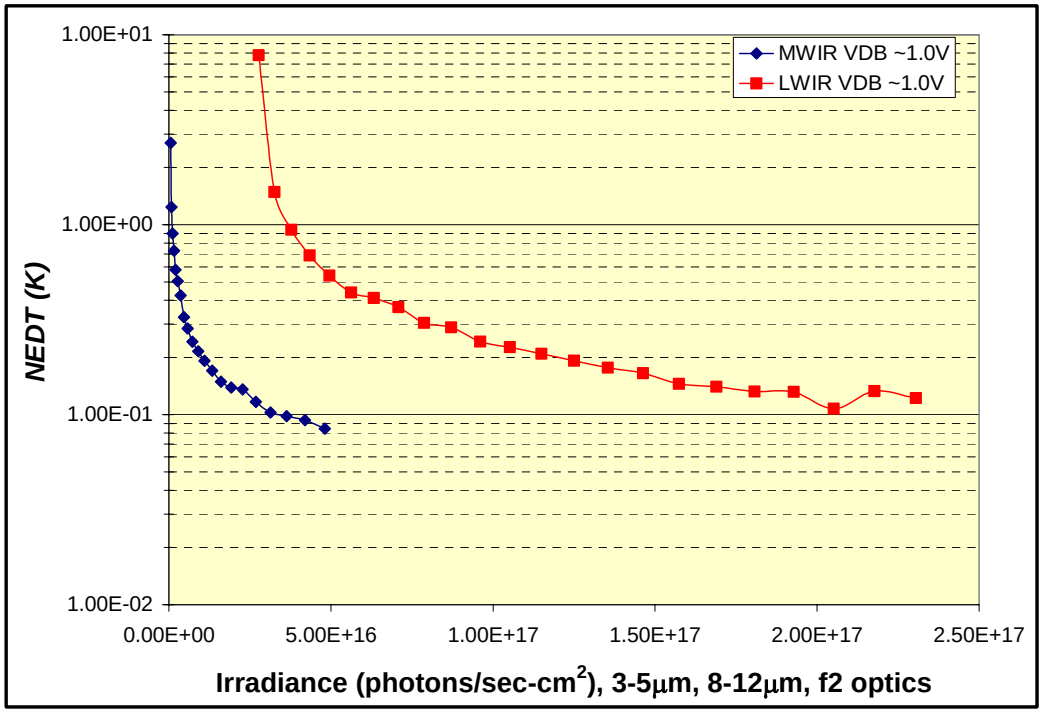

Figure 60. MWIR and LWIR NEDT at V_{DB} ~1.0V and 77K

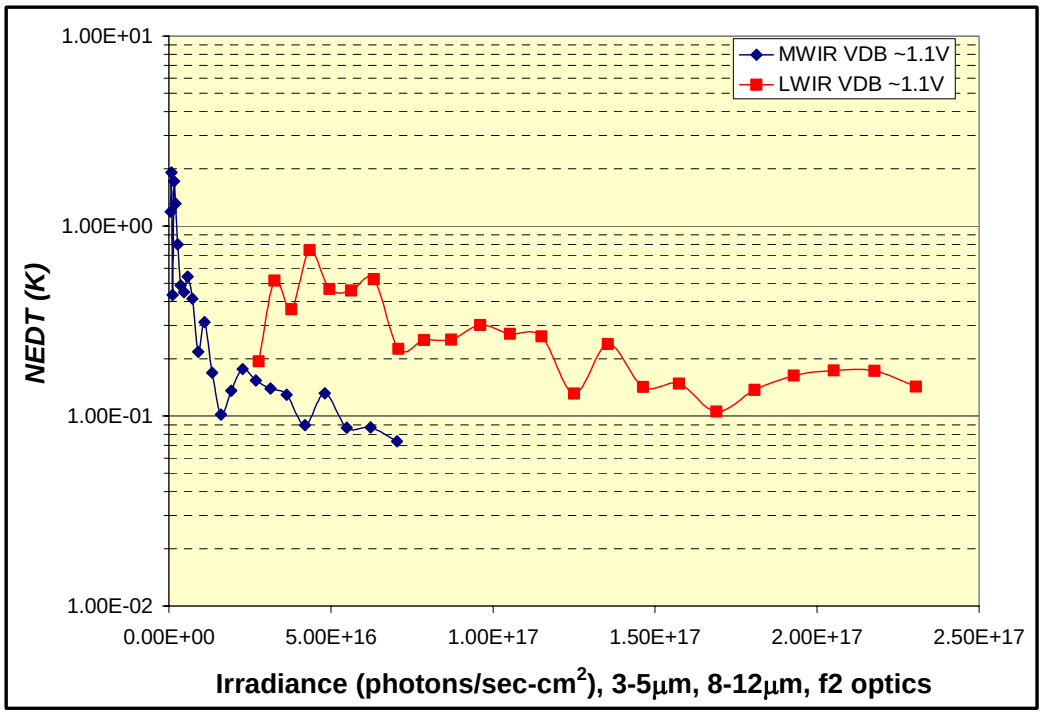

Figure 61. MWIR and LWIR NEDT at V_{DB} ~1.1V and 77K

References

[1] **Berryman, K.W., et al**, Applied Physics Letters, 1997, Volume 70, Number 14

[2] **Bhattachara, P., et al,** *Research propels quantum dots forward,* Laser Focus World, May 2005

[3] **Campbell, J and Madhukar, A.**, *Quantum Dot Infrared Photodetectors,* Proceedings of the IEEE, (29 November, 2006)

[4] **Dereniak, E. L. and Boreman, G.**, *Infrared Detectors and Systems,* (Wiley, New York, 1996)

[5] **Hsieh, C.C., et al**, *Focal-Plane-Arrays and CMOS Readout Techniques of Infrared Imaging Systems*, IEEE Transactions on Circuits and Systems for Video Technology, Vol 7, No 4, August 1997

[6] **Kasap, S.O.**, *Optoelectronics and Photonics: Principles and Practices*, (Prentice Hall, New Jersey, 2001)

[7] **Kim, S., et al**, Applied Physics Letters, 1998, Volume 73, Number 7

[8] **Kozlowski, et al**, SPIE Infrared Detectors and Focal Plane Arrays, Vol 1308 (1990)

[9] **Krishna, et al**, Journal of Applied Physics D: Applied Physics, 2005, Volume 38

[10] **Levine, B.F., et al**, Journal of Applied Physics, 1993, Volume 74, Number 8

[11] **Liu, H.C., et al**, Applied Physics Letters, 2001, Volume 78, Number 1

[12] **Maimon, S., et al**, Applied Physics Letters, 1998, Volume 73, Number 14

[13] **Nelson, M.D., et al**, *General noise processes in hybrid infrared focal plane arrays*, SPIE Optical Engineering, Vol 30, No 11, November 1991

[14] **Pan, D. and Towe, E.**, Applied Physics Letters, 1998, Volume 73, Number 14

[15] **Rogalski, A.**, Journal of Applied Physics, 2003, Volume 93 , Number 8

[16] **Rogalski, A.,** Proceedings of SPIE, 2006, Volume 6206

[17] **Rogalski, A.,** *Third generation infrared detectors*, Proceedings of the Symposium on Photonics Technologies for 7th Framework Program, 2006

[18] **Singh, J.**, *Semiconductor Devices: Basic Principles*, (Wiley, New York, 2001)

[19] **Smith, E.P.G., et al**, *Fabrication and Characterization of Two-Color Midwavelength/Longwavelength HgCdTe Infrared Detectors*, Journal of Electronic Materials, Vol 35, No 6, 2006

[20] **Sobering, T.J. and Green, J. L.**, *Reset Noise in Multiplexed Photodiode Arrays*, (March 2004)

[21] **Swanson, R. and Meidl, J.D.**, *Ion Implanted Complementary MOS Transistors in Low-Voltage Circuits*, IEEE Journal of Solid-State Circuits SC-7(2), 146-153 (April 1972)

[22] **Varley, E., Lenz, M., et al**, *Single bump, two-color quantum dot camera*, Applied Physics Letters, 2007, Volume 91, Number 8

[23] **Veeco Instruments Inc**, *Resources-Epitaxial Equipment: Growth Information*, (accessed 8 August 2007) <http://www.veeco.com/library/resources_view_sub.php?id=32>

[24] **Vincent, J.D.**, *Fundamentals of Infrared Detector Operation & Testing*, (Wiley, New York, 1990)

[25] **Wikipedia**, http://en.wikipedia.org/wiki/Infrared (accessed 8 August 2007)